Monthly Notices
of the
ROYAL ASTRONOMICAL SOCIETY

Mon. Not. R. Astron. Soc. **426,** 2917–2943 (2012) doi:10.1111/j.1365-2966.2012.21879.x

The Elephant Trunk Nebula and the Trumpler 37 cluster: contribution of triggered star formation to the total population of an H II region

Konstantin V. Getman,[1⋆] Eric D. Feigelson,[1,2] Aurora Sicilia-Aguilar,[3] Patrick S. Broos,[1] Michael A. Kuhn[1] and Gordon P. Garmire[1]

[1]*Department of Astronomy & Astrophysics, 525 Davey Laboratory, The Pennsylvania State University, University Park, PA 16802, USA*
[2]*Center for Exoplanets and Habitable Worlds, The Pennsylvania State University, University Park, PA 16802, USA*
[3]*Departamento de Fisica Terica, Universidad Aut noma de Madrid, Cantoblanco 28049, Madrid, Spain*

Accepted 2012 August 6. Received 2012 August 2; in original form 2012 April 12

ABSTRACT

Rich young stellar clusters produce H II regions whose expansion into the nearby molecular cloud is thought to trigger the formation of new stars. However, the importance of this mode of star formation is uncertain. This investigation seeks to quantify triggered star formation (TSF) in IC 1396A (aka the Elephant Trunk Nebula), a bright-rimmed cloud (BRC) on the periphery of the nearby giant H II region IC 1396 produced by the Trumpler 37 cluster. X-ray selection of young stars from *Chandra X-ray Observatory* data is combined with existing optical and infrared surveys to give a more complete census of the TSF population. Over 250 young stars in and around IC 1396A are identified; this doubles the previously known population. A spatio-temporal gradient of stars from the IC 1396A cloud towards the primary ionizing star HD 206267 is found. We argue that the TSF mechanism in IC 1396A is a radiation-driven implosion process persisting over several million years. Analysis of the X-ray luminosity and initial mass functions indicates that >140 stars down to 0.1 $M_{\odot}$ were formed by TSF. Considering other BRCs in the IC 1396 H II region, we estimate the TSF contribution for the entire H II region exceeds 14–25 per cent today, and may be higher over the lifetime of the H II region. Such triggering on the periphery of H II regions may be a significant mode of star formation in the Galaxy.

Key words: protoplanetary discs – stars: formation – open clusters and associations: individual: IC 1396 – open clusters and associations: individual: Trumpler 37 – ISM: individual objects: Elephant Trunk Nebula – X-rays: stars.

1 INTRODUCTION

1.1 Motivation

A long-standing issue in Galactic star formation is: how much star formation relies on spontaneous gravitational collapse of cold clouds? *versus* how much star formation relies on collapse 'triggered' by the imposition of external forces? Triggered star formation (TSF) may play roles on large scales from compression by Galactic spiral arms, on meso-scales from compression by supernova remnant superbubbles in starburst complexes, and on small scales from compression by expanding H II regions (Elmegreen & Palous 2007). It has long been recognized that star formation in molecular clouds can be triggered by ionization or shock fronts produced by nearby massive stars (Elmegreen & Lada 1977). Two major mechanisms for triggering by expanding H II regions have been widely discussed: the Radiation Driven Implosion (RDI) model and the Collect and Collapse (C&C) model.

In the RDI model, the expanding OB ionization front ablates the surface of surrounding pre-existing cloudlets producing bright-rimmed clouds (BRCs), often with cometary structures, and driving inwards a compressional shock that induces star formation. Discussed since the 1980s, RDI now has well-developed hydrodynamical calculations showing the viability of TSF on time-scales ∼ 0.1 Myr (Kessel-Deynet & Burkert 2003; Miao et al. 2009; Bisbas et al. 2011, and references therein).

Observationally, two types of BRCs can be distinguished: relatively massive cloudlets with widths of $w > 0.5$–0.7 pc, which are often found to harbour more than a few stars at their tips; and thin ($w < 0.5$ pc) elongated pillar-like structures with a few or no stars at their tips (Chauhan et al. 2011). According to the RDI model, this distinction may reflect different evolutionary stages of BRCs with narrow pillars interpreted as the last vestiges of the photoevaporated

⋆E-mail: gkosta@astro.psu.edu

and dispersed cloudlet that has insufficient amount of remaining gas to form new stars (Bisbas et al. 2011). Alternative explanations for the thin elongated pillars involve hydrodynamic instabilities in ionization fronts (Mizuta et al. 2006; Whalen & Norman 2008) or ionization of large turbulent clouds without pre-existing cloudlets (Gritschneder et al. 2010, and references therein).

In most cases, molecular, infrared (IR) and Hα surveys of BRCs trace only the most recently formed stars (e.g. Sugitani, Tamura & Ogura 1995; Ogura, Sugitani & Pickles 2002; Urquhart, Morgan & Thompson 2009). While longer wavelength surveys select principally the youngest stars undergoing accretion from dusty discs, X-ray surveys efficiently select young stars due to enhanced magnetic reconnection flaring that extends to the main sequence (Feigelson 2010). In a few cases, *Chandra* observations have added the disc-free pre-main-sequence (PMS) populations to TSF clouds (e.g. Getman et al. 2007, 2009). Triggered BRCs often show embedded mid-IR (MIR) sources denoting protostars, while Hα, *JHK*, and X-ray surveys reveal small clusters of discy and disc-free PMS stars within and in front of the bright rim.[1] In a few cases, spatial-age gradients in the stellar population are clearly seen where the youngest stars are embedded and older stars are aligned towards the ionizing sources (e.g. Getman et al. 2007; Ogura et al. 2007; Ikeda et al. 2008; Getman et al. 2009). This directly supports the RDI mechanism and implies that the existing clouds have been actively forming stars for more than 1 Myr.

In the C&C model, ionization and wind shock fronts sweep up neutral material into a dense shell that becomes gravitationally unstable and fragments. Individual stars or entire massive clusters may form inside these fragments. The theory is moderately developed (Whitworth et al. 1994; Hosokawa & Inutsuka 2006; Dale, Bonnell & Whitworth 2007a) and may explain a number of spectacular examples of embedded clusters found around H II regions using long-wavelength (millimetre to near-IR) observations (Deharveng et al. 2003; Zavagno et al. 2006, 2007). They find a central ionizing star with a roughly spherical H II region surrounded by a shell of dense molecular gas with dense fragments harbouring young stellar objects (YSOs). However, recent smoothed particle hydrodynamics (SPH) simulations by Walch et al. (2011) show that if an H II region expands into a clumpy molecular cloud, then the production of a molecular shell with dense massive fragments does not require the C&C mechanism. Instead, TSF would take place through simultaneous enhancement of density and global radiation-driven implosion of pre-existing molecular clumps.

Star formation triggered by H II regions may be very common. The *Spitzer*/GLIMPSE survey finds $\sim$10 MIR bubbles per deg^2 throughout the Galactic disc (Churchwell et al. 2006; Simpson et al. 2012). Deharveng et al. (2010) show that most of these bubbles enclose H II regions ionized by O-B2 stars, many are surrounded by cold dust shells and many have bright-rimmed dust condensations protruding inside the H II region. 26 per cent of the dust shell condensations have ultracompact H II (UCH II) regions and/or methanol masers, likely indicating triggering of massive star formation. Based on the cross-correlation of the positions of the MIR shells with the positions of the very bright and red YSOs from the Red MSX Source (RMS) catalogue, Thompson et al. (2012) estimate that the formation of 14–30 per cent of massive stars in the Milky Way could be triggered by expanding H II regions.

[1] Henceforth, the term 'in front of' refers to the region between a globule and an ionizing star(s) in two-dimensional projection, and not the region between the observer and the globule.

Due to violent energy feedback from massive stars in large star-forming complexes and individual H II regions, the geometry, conditions and history of star formation are often difficult to ascertain. The principal signatures of small-scale TSF – a star cluster in and around the cloudlet on the periphery of an expanding H II region – may be erased through removal of the cloudlet by stellar winds and ultraviolet (UV) radiation, or the kinematic dispersal of the unbound cluster within less than a few million years. Thus, it is often difficult to identify sites of TSF and to quantify the impact of triggering processes. IC 1396 is a nearby ($D \sim 870$ pc; Contreras et al. 2002), large ($\sim$12 pc in radius) shell-like H II region, where traces of recent TSF are still evident (Kun, Kiss & Balog 2008, and references therein). The goal of this study is to identify, understand and quantify the triggered stellar population in the central part of the region associated with the largest BRC, IC 1396A (Elephant Trunk Nebula), and to estimate the contribution of TSF to the total stellar population in both the central part and, with some additional assumptions, the entire H II region.

1.2 The target: IC 1396A globule

The IC 1396 H II region, Sh 2-131 at (l, b) = (99.°3, 3.°7), is excited mainly by the O6.5f star HD 206267 located at the centre of the region in the 4-Myr-old cluster Trumpler 37 (Sicilia-Aguilar et al. 2005, hereafter SA05). IC 1396 has a rich population of >20 bright-rimmed and cometary globules seen in silhouette against the emission nebula (Sugitani, Fukui & Ogura 1991; Froebrich et al. 2005, and Fig. 1 here). Many of the clouds reside on the large molecular shell surrounding the H II region, which expands at a speed of 5 km s^{-1} with an inferred expansion time around 2.5 Myr (Patel et al. 1995). Sites of possible star formation have been identified in/around at least several globules (e.g. Schwartz, Wilking & Giulbudagian 1991; Ogura, Sugitani & Pickles 2002; Froebrich et al. 2005) including sites of substantial star formation in IC 1396N (Nisini et al. 2001; Getman et al. 2007; Beltrán et al. 2009; Choudhury, Mookerjea & Bhatt 2010), SFO 37 (Ikeda et al. 2008) and IC 1396A (Reach et al. 2004; SA05; Sicilia-Aguilar et al. 2006; Morales-Calderón et al. 2009; Barentsen et al. 2011).

Lying $\sim$15 arcmin ($\sim$3.7 pc projected distance) west of HD 206267, IC 1396A is the BRC closest on the sky to HD 206267. Its optical rim is the brightest of all rims and the cloud is thus likely to be the physically closest to HD 206267 (Weikard et al. 1996). Following Weikard et al. (1996) we designate the two brightest features of the rim as Rim A located in front of the >1 pc diameter head of the globule and Rim Aa located farther west at the shoulder (trunk) of the cloud (Fig. 1). The part of the cloud behind Rim Aa has its own designation: SFO 36 (Sugitani et al. 1991). A 0.3-pc-diameter cavity in the molecular cloud is present in the head of the globule produced by the Herbig Ae star LkHa 349 (Hessman et al. 1995). Outside this 'hole', the globule is optically thick ($A_V \sim 10$ mag) with molecular mass $\sim 200\,M_\odot$ (Patel et al. 1995; Weikard et al. 1996).

Early *Spitzer* images revealed both bright diffuse MIR emission and 17 Class II/I stars in the IC 1396A globule (Reach et al. 2004, their fig. 2). A spectacular multiband movie of the cloud was one of the first press releases of the *Spitzer* mission.[2] SA05 and Sicilia-Aguilar et al. (2006, hereafter SA06) combined new deeper and wider area *Spitzer* photometry with optical photometry and

[2] The press release can be found at http://www.spitzer.caltech.edu/images/1058-ssc2003-06b-Dark-Globule-in-IC-1396.

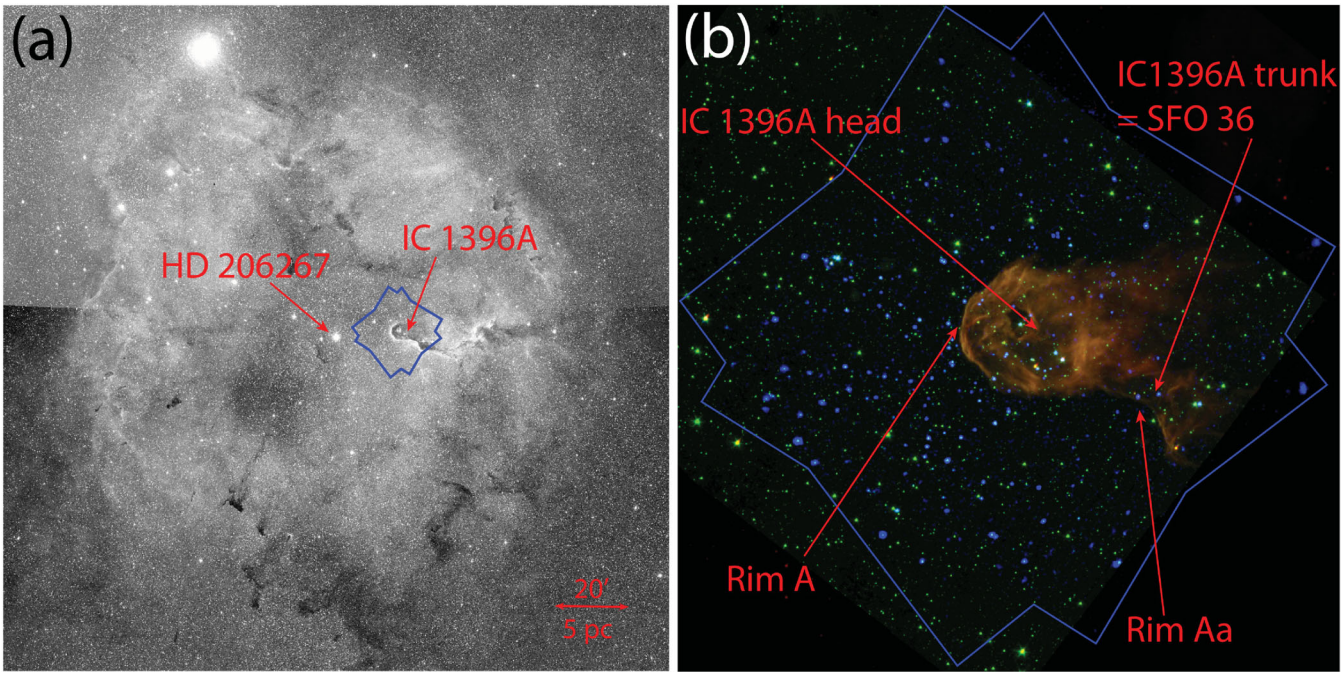

Figure 1. Panel (a): a $3 \times 3\,\mathrm{deg}^2$ image of the emission nebula IC 1396 from the Digitized Sky Survey (DSS). The primary ionizing source of the region, the O6 star HD 206267, and the bright-rimmed globule IC 1396 are marked in red. The blue polygon outlines the ACIS field centred on IC 1396A. Panel (b): close-up, combined X-ray and IR image of IC 1396A. The adaptively smoothed *Chandra*-ACIS image in the 0.5–8.0 keV band (blue) is superposed on the *Spitzer*-IRAC composite image in the 3.6 μm (green) and 8.0 μm (red) bands. The ACIS field is outlined in blue; the head and the trunk of the cloud are marked in red. The positions of the two brightest features of the ionized optical rim in front of the cloud are marked in red as Rims A and Aa. North is up, east is to the left.

spectroscopy to reveal a rich lightly obscured population of >200 Hα emission and/or Li 6707 Å absorption stars. The population is a mixture of ∼4 Myr old members of the central Trumpler 37 cluster and ∼1 Myr stars spatially concentrated in an arc in front of the globule (see fig. 11 in SA05). In addition, ∼50 heavily obscured IR-excess-selected objects were found inside the cloud (SA06). Deeper *Spitzer*-IRAC maps from the time-series monitoring of the globule (Morales-Calderón et al. 2009, hereafter MC09) uncovered an additional dozen heavily embedded Class I/II YSOs. The spatial distribution of 65 discy members in/around the globule is shown in fig. 16 of MC09. Recently, using the data from the INT Photometric H-Alpha Survey, Barentsen et al. (2011, hereafter B11) identified about two dozen low-mass, high-accretion T Tauri systems spatially concentrated in an arc in front of the globule (see fig. 18a in B11). About half of these were newly discovered stellar members of the region. Spatial clustering of optical stars with younger ages and increasing accretion rates away from the ionizing star HD 206267 (SA05; B11) led SA05 and B11 to propose the presence of a stellar population in front of the IC 1396A globule whose formation has been triggered by HD 206267. Thus, several high-sensitivity optical and MIR surveys have revealed a few hundred young stars in the Trumpler 37 region, with the youngest concentrated within and around IC 1396A.

As X-ray emission from PMS stars is based on enhanced solar-type magnetic reconnection events rather than disc or accretion processes, X-ray selection delivers rich and clean samples of discless stars missed by Hα and IR selection (Feigelson 2010). Using archived X-ray *Chandra* grating data, Mercer et al. (2009) identified 22 new PMS stars around HD 206267, more than doubling the number of previously reported young stars in the central $10 \times 8\,\mathrm{arcmin}^2$ area of Trumpler 37. We present here the identification of >130 previously unknown members of the Trumpler 37/IC 1396A stellar populations, using new X-ray and optical observations with archived *Spitzer* data. The *Chandra* and the auxiliary *Spitzer* and optical Fred Lawrence Whipple Observatory (FLWO)/LAICA data are described in Section 2. Identification of X-ray sources with optical–IR counterparts and membership classification are considered in Section 3. Classification of disc-bearing and discless X-ray-emitting YSOs is provided in Section 3.3, and the discovery of a new population of non-*Chandra* IR-excess members is given in Section 4. We then estimate the global properties of the Trumpler 37/IC 1396A stellar populations including age distribution (Section 5), spatial structure (Section 6), X-ray luminosity functions (XLFs) and initial mass functions (IMFs; Section 7). We end with a discussion of the implications for understanding and quantifying TSF in the region (Section 8).

2 *Chandra*-ACIS, *Spitzer*-IRAC AND OPTICAL OBSERVATIONS

2.1 X-ray data

The current project consists of two *Chandra*-ACIS (Weisskopf et al. 2002; Garmire et al. 2003) X-ray observations of IC 1396A, a Guaranteed Time observation (ObsID No. 11807 obtained on 2010 March 31; PI: Garmire) and a Guest Observer observation (ObsID No. 10990 obtained on 2010 June 9; PI: Getman). Both observations

were pointed at the head of the globule but had different roll angles.[3] For each observation, we consider here only results arising from the imaging array (ACIS-I) of four abutted 1024 × 1024 pixel front-side illuminated charge-coupled devices (CCDs) covering about 17 × 17 arcmin^2 on the sky. The S2 and S3 detectors in the spectroscopic array (ACIS-S) were also operational, but as the telescope point spread function (PSF) is considerably degraded far off-axis, the S2-S3 data are omitted from the analysis. The overlapping field of the two observations achieved 59 ks of exposure with no data losses or background flaring due to solar activity.

Data reduction follows procedures similar to those described in detail by Broos et al. (2010, 2011). Level 1 event data were calibrated and cleaned using mostly standard methods and tools (CIAO version 4.3; CALDB version 4.4.0). Event positions were adjusted to better align with the Naval Observatory Merged Astrometric Data (NOMAD) set catalogue (Zacharias et al. 2004). The effective PSF was slightly improved by removing a pixel randomization that was historically added to ACIS event positions, and by applying a sub-pixel position estimation algorithm (Li et al. 2004). A custom bad pixel table was used to slightly increase point source sensitivity. Instrumental background events were identified and removed using an aggressive algorithm when searching for sources and using an algorithm with few false positives when extracting sources (Broos et al. 2010, their fig. 1).

Detection of point sources is performed using both the wavelet transform method (Freeman et al. 2002) and the Lucy–Richardson image reconstruction algorithm (Broos et al. 2010, their section 4.2); the latter is better suited for resolving closely spaced sources. Updated position estimates, photometry, and spectra were obtained for candidate sources using the ACIS EXTRACT (AE) software package[4] (Broos et al. 2010, 2012).

Some of the inferred properties, such as X-ray net counts (NC), background counts (BC), median energy (ME) and apparent flux (F_X) for the full (0.5–8) keV energy band, as well as the p value for the no-source hypothesis (PbNoSrc; Broos et al. 2010, their section 4.3 and appendix B), are provided in Table 1. Similar to the *Chandra* catalogue of X-ray sources in the Carina Nebula (Broos et al. 2011), our list of candidate sources in IC 1396A is trimmed to omit sources with fewer than 3 total source counts (NC + BC < 3) and the probability for being a background fluctuation greater than 1 per cent (PbNoSrc > 0.01).

Our final catalogue comprises 415 X-ray sources (Table 1). We expect that roughly half of these sources are extragalactic with extremely optically faint counterparts (Section 3.2), and the rest are young stars associated with the Trumpler 37 and IC 1396A star-forming regions.

2.2 IRAC Data

To obtain MIR photometry for X-ray objects and to identify and measure MIR photometry for additional non-*Chandra* discy stars that were missed in previous studies of the region, we have reduced the archived *Spitzer*-IRAC (Fazio et al. 2004) data from a Guaranteed Time observation of the programme #37 (PI: Fazio). The same

[3] The aim points of the observations were $21^h36^m51\overset{s}{.}5$, $+57^\circ30'51\overset{''}{.}3$ (J2000) and $21^h36^m47\overset{s}{.}6$, $+57^\circ30'43\overset{''}{.}3$ (J2000) for ObsIDs 11807 and 10990, respectively. The roll angles were $52\overset{\circ}{.}4$ and $121\overset{\circ}{.}2$ for ObsIDs 11807 and 10990, respectively.

[4] The AE software package and User's Guide are available at http://www.astro.psu.edu/xray/acis/acis_analysis.html.

Table 1. Basic X-ray source properties. This table is available in its entirety as Supporting Information with the electronic version of the article. A portion is shown here for guidance regarding its form and content. Source net counts, background counts, median energy and apparent photometric flux are given for the full (0.5–8) keV band. Column 1: X-ray source number. Column 2: IAU designation. Columns 3 and 4: right ascension and declination for epoch J2000.0 in degrees. Column 5: 1σ error circle around the source position. Column 6: average off-axis angle for the two merged X-ray observations. Column 7: source net counts in merged apertures and their 1σ upper errors. Column 8: observed background counts in merged apertures. Column 9: average PSF fraction for merged observations (at 1.5 keV) enclosed within the source aperture. Column 10: smallest of the three p values (for the full, soft and hard energy bands) for the no-source hypothesis. Column 11: effective exposure time. Columns 12: smallest p value for the one-sample K–S statistic under the no-variability null hypothesis within a single observation. Column 13: p value for the one-sample K–S statistic under the no-variability null hypothesis over the combined observations. Columns 14 and 15: X-ray median energy and apparent photometric flux.

S. No.	CXOIC1396A	RA	Dec.	PosErr	Θ	NC	BC	PSF	PbNoSrc	EffExp	PbVar1	PbVar2	ME	F_X
		(°)	(°)	(arcsec)	(arcmin)	(counts)	(counts)			(ks)			(keV)	(photon cm^{-2} s^{-1})
(1)	(2)	(3)	(4)	(5)	(6)	(7)	(8)	(9)	(10)	(11)	(12)	(13)	(14)	(15)
1	213529.03+573412.3	323.871000	57.570087	0.5	11.1	130.9 ± 12.9	10.1	0.90	0.0E+00	28.0	1.8E−01	1.8E−01	2.3	2.6E−05
2	213532.88+572846.9	323.887026	57.479703	0.3	10.8	271.5 ± 17.9	11.5	0.91	0.0E+00	29.1	3.2E−01	3.2E−01	1.5	4.9E−05
3	213537.29+572842.0	323.905409	57.478345	1.2	10.2	16.3 ± 6.3	10.7	0.91	6.7E−07	29.1	6.9E−01	6.9E−01	1.4	2.9E−06
4	213538.86+573032.7	323.911957	57.509103	0.9	9.8	27.7 ± 7.2	9.3	0.90	1.3E−12	28.9	8.9E−01	8.9E−01	2.0	5.0E−06
5	213539.72+573127.5	323.915509	57.524320	1.1	9.1	13.7 ± 5.6	6.3	0.89	6.2E−07	28.8	6.2E−01	6.2E−01	3.8	2.5E−06
6	213541.87+573252.8	323.924497	57.548001	1.2	9.1	9.3 ± 5.0	5.7	0.89	1.6E−04	28.9	9.9E−01	9.9E−01	2.9	1.7E−06
7	213542.94+573334.8	323.928939	57.559685	0.9	9.1	19.1 ± 6.2	6.9	0.90	4.9E−12	28.9	6.0E−01	6.0E−01	1.1	3.4E−06
8	213543.96+572955.9	323.933171	57.498871	0.8	8.9	21.4 ± 6.8	10.6	0.90	1.4E−08	48.4	2.0E−01	2.4E−01	1.7	2.2E−06
9	213545.27+573326.5	323.938631	57.557375	1.0	8.8	11.9 ± 5.4	6.1	0.90	4.2E−07	27.7	7.7E−01	7.7E−01	1.4	2.2E−06
10	213550.45+573547.5	323.960213	57.596543	0.4	9.2	110.5 ± 11.8	4.5	0.90	0.0E+00	20.7	2.3E−01	2.3E−01	1.5	2.7E−05
...	...	...	...	...	...	...	...	...	...	...	...	...	...	...

observation has been presented in SA06 and Sicilia-Aguilar et al. (2011, hereafter SA11). The SA06 data had been reduced using old calibration and flat-fielding information, and the photometry for sources with highly non-uniform background was additionally affected by the choice of large source extraction apertures. Given the improvement of the pipeline and calibration since then, SA11 have re-reduced the data and redone the photometry for a selected sample of YSOs. Since both the SA06 and SA11 catalogues lack photometry measurements for the bulk of the X-ray sources, reanalysis of the data is in order.

The observation was obtained on 2003 December 20 with the IRAC detector in all four IRAC channels, 3.6, 4.5, 5.8 and 8.0 μm. Two adjacent fields subtending $\sim 37 \times 42$ arcmin^2 in channel pairs 3.6/5.8 μm and 4.5/8.0 μm were centred on Trumpler 37. These fields were imaged with an 8 × 9 mosaic of adjacent positions separated by 280 arcsec; individual exposures were taken at five dithered positions for each of the 72 cells of the mosaic. The images were taken in the high-dynamic-range mode with 30 and 1.2 s frame time exposures. To reduce unnecessary data processing we have analysed only a portion of the original data that encompasses the *Chandra*-ACIS field with a coverage of $\sim 19 \times 19$ arcmin^2 area in all four channels centred on Rim A of the IC 1396A globule. This covers 93 per cent of the ACIS field omitting its north-western and south-western edges.

Basic calibrated data (BCD) products from Spitzer Science Center's IRAC pipeline version S18.18.0 were automatically treated with the WCSMOSAIC IDL package developed by R. Gutermuth from the IRAC instrumental team. Starting with BCD products, the package mosaics individual exposures while treating bright source artefacts, cosmic-ray rejection, distortion correction, subpixel offsetting, and background matching (Gutermuth et al. 2008). We selected a plate scale of 0.86 arcsec for the reduced IRAC mosaics, which is the native scale divided by $\sqrt{2}$.

Aperture photometry of IRAC sources was obtained using the IRAF task PHOT. Circular apertures with radius of 2, 3 and 4 pixels (1.72, 2.58 and 3.44 arcsec, respectively) are assigned, with larger apertures favoured for uncrowded sources and smaller apertures favoured for crowded sources. Using the IRAC PSF for the [3.6] band resampled to a plate scale of 0.86 arcsec, pairs of sources are simulated with wide ranges of source separations, orientations and flux ratios to derive the flux contribution from a nearby source within 2-, 3- and 4-pixel apertures as a function of separation angle and flux ratio (Kuhn et al., in preparation). For the real sources, their photometry is derived using 2-, 3- and 4-pixel source apertures, and we report photometry from the largest aperture for which the expected contamination from a nearby source is less than 5 per cent. A source aperture radius of 4 pixels was used for most of the X-ray sources and non-*Chandra*-selected sources of interest (Section 4). The cases for which the expected contamination is >10 per cent in the smallest 2-pixel aperture are flagged in Table 2 as '2c'.

The background in the region is highly non-uniform due to the contribution by the PSF cores and wings of multiple neighbouring sources often superimposed on top of the spatially variable diffuse emission. For all IRAC sources, the aperture photometry was performed for two different sizes of sky annuli, 4- and 1-pixel-wide sky annuli adjoining source extraction regions. The former, closer in size to the 'standard' sky annuli recommended in the IRAC Instrument Handbook, collects higher numbers of sky pixels offering smaller statistical uncertainties but with the danger of increased systematic error due to sampling wrong background. The latter is chosen in accordance with the strategy of, for example, Lada et al. (2006), Luhman et al. (2008), Getman et al. (2009) and K. Luhman

Table 2. Optical and IR photometry of X-ray sources. This table is available in its entirety as Supporting Information with the electronic version of the article. A portion is shown here for guidance regarding its form and content. Column 1: X-ray source number. Columns 2–5: optical $V_{\rm FLWO}$, $I_{\rm C,FLWO}$, $V_{\rm LAICA}$, and $I_{\rm J,LAICA}$ magnitudes. Columns 6–9: 2MASS $JHK_{\rm s}$ magnitudes, and 2MASS photometry quality and confusion-contamination flags. Columns 10–14: IRAC magnitudes, and a digital flag giving photometric apertures and the level of source contamination from nearby sources and nebular IR emission: '3' and '4' – 3-pixel (2.6 arcsec) and 4-pixel (3.46 arcsec) apertures with contaminating flux from a neighbouring source of no more than 5 per cent; '2' and '2c' – 2-pixel (1.73 arcsec) apertures with possible contaminating flux of <10 and >10 per cent, respectively.

S. No.	$V_{\rm FLWO}$	$I_{\rm C,FLWO}$	$V_{\rm LAICA}$	$I_{\rm J,LAICA}$	J	H	$K_{\rm s}$	F2	[3.6]	[4.5]	[5.8]	[8.0]	F3
	(mag)	(mag)	(mag)	(mag)	(mag)	(mag)	(mag)		(mag)	(mag)	(mag)	(mag)	
(1)	(2)	(3)	(4)	(5)	(6)	(7)	(8)	(9)	(10)	(11)	(12)	(13)	(14)
1	–	–	–	–	–	–	–	–	–	–	–	–	–
2	–	–	–	–	12.64 ± 0.03	11.82 ± 0.03	11.56 ± 0.02	AAA000	–	–	–	–	–
3	–	–	–	–	13.65 ± 0.03	12.95 ± 0.03	12.71 ± 0.03	AAA000	–	–	–	–	–
4	–	–	–	–	–	–	–	–	–	–	–	–	–
5	–	–	–	–	–	–	–	–	16.20 ± 0.06	15.64 ± 0.05	–	–	2
6	13.44 ± 0.00	12.37 ± 0.00	13.57 ± 0.00	12.01 ± 0.00	11.49 ± 0.03	11.18 ± 0.03	11.07 ± 0.03	AAA000	10.92 ± 0.01	10.90 ± 0.02	10.92 ± 0.04	10.75 ± 0.03	3
7	–	–	19.48 ± 0.01	15.51 ± 0.00	14.30 ± 0.04	13.44 ± 0.03	13.07 ± 0.04	AAA000	12.53 ± 0.00	12.28 ± 0.00	12.13 ± 0.01	11.54 ± 0.04	4
8	–	–	19.44 ± 0.01	16.48 ± 0.00	14.22 ± 0.04	13.38 ± 0.04	13.17 ± 0.04	AAA000	12.86 ± 0.05	12.82 ± 0.06	12.65 ± 0.05	–	2
9	19.50 ± 0.08	16.41 ± 0.01	19.36 ± 0.01	15.71 ± 0.00	14.61 ± 0.04	13.87 ± 0.04	13.66 ± 0.04	AAA000	13.34 ± 0.01	13.24 ± 0.01	13.26 ± 0.07	–	4
10	–	–	–	–	12.86 ± 0.03	12.28 ± 0.04	12.11 ± 0.03	AAAcc0	–	–	–	–	–
…	…	…	…	…	…	…	…	…	…	…	…	…	…

(private communication) who attempt to sample the actual sky present within the source extraction region. For background selection, the optimal balance between proximity and the number of background pixels is not obvious.

We adopt zero-point magnitudes (ZP) of 19.670, 18.921, 16.855 and 17.394 in the 3.6, 4.5, 5.8 and 8.0 μm bands, respectively, where $M = -2.5\log(\mathrm{DN/s}) + \mathrm{ZP}$ (Reach et al. 2005). Since our plate scale and the extraction apertures have custom sizes, the aperture correction values are calculated here using the current data as described by Luhman et al. (2010). The calculations are based on the comparison of the photometric measurements for the relatively isolated, bright and unsaturated sources obtained for the source and sky regions of different sizes including large 14 pixel (∼10 native pixel) extraction regions that are similar in size to those used in the calibrations of Reach et al. (2005). The total aperture corrections applied to our measurements in the case of the 4-pixel background annulus are: 0.213, 0.184, 0.218 and 0.416 mag in the case of the 4-pixel source aperture; 0.441, 0.367, 0.698 and 0.949 mag in the case of the 3-pixel source aperture; and 0.829, 0.955, 1.319 and 1.105 mag in the case of the 2-pixel source aperture in the 3.6, 4.5, 5.8 and 8.0 μm bands, respectively. The total aperture corrections applied to our measurements in the case of the 1-pixel background annulus are: 0.174, 0.171, 0.161 and 0.180 mag in the case of the 4-pixel aperture; 0.387, 0.304, 0.496 and 0.653 mag in the case of the 3-pixel aperture; and 0.637, 0.714, 0.976 and 0.868 mag in the case of the 2-pixel aperture in the 3.6, 4.5, 5.8 and 8.0 μm bands, respectively. The reported photometric errors include statistical errors in the source and background emission and a 2 per cent uncertainty in the calibration of IRAC (Reach et al. 2005). For further analyses we retain IRAC sources with signal-to-noise ratio >3 in both the [3.6] and the [4.5] bands, and the photometry is reported if signal-to-noise ratio >3.

For all extracted IRAC sources, we compare their photometric measurements performed with 1 pixel and 4 pixel background annuli. Fig. 2 exemplifies such a comparison for the [3.6] band. For the sources with source apertures 4 pixel (orange), 3 pixel (blue) and 2 pixel (green) the distributions of the magnitude differences typically have small biases of <0.02–0.05 mag and dispersions of <0.04–0.2 mag increasing towards the fainter magnitudes and longer wavelengths. Both the effect of the finite number of background pixels and the possible physical mistakes the two methods are making could be the cause of the magnitude biases and spreads. In the case of the most crowded sources, with the apertures '2c' (red), the bias and dispersion are higher, <0.02–0.08 mag and <0.1–0.4 mag, respectively. The nature of this bias is unclear. For example, if a neighbour lies within the 1 pixel aperture, then the larger 4 pixel aperture would dilute the light from this neighbour, shifting the photometry in the observed direction. For the X-ray subsample of '2c' sources, the bias appears only in the range of [3.6] > 16 mag characteristic of objects unrelated to this relatively close star-forming region (Section 3.2). Performing the disc classification based on spectral energy distributions (SEDs) as described in Section 3.3, we find that the choice of the background aperture appears to have a tiny effect on SED shapes and no discernible effect on the disc classification for all X-ray YSOs. Since there is no evident preference for either background annulus size, we publish the photometry from the method with the 1-pixel-wide background annuli, which produces conservatively large statistical errors. Derived IRAC photometric measurements for 242 X-ray sources are given in Table 2.

For the objects in common with MC09 we compare our photometric measurements with the time-averaged measurements of MC09 that are based on new deeper *Spitzer*-IRAC exposures. Fig. 3 exemplifies such a comparison for the [3.6] band. The source sample here is relatively bright ([3.6] < 14 mag), so the magnitude differences are not affected by the choice of our background apertures. The magnitude differences have small biases of 0.02–0.03 mag and dispersions of 0.22–0.25 mag. About 60 per cent of the sources considered here are MIR variable. Since the sources are relatively bright, variability rather than photometric uncertainty is likely the major cause of the magnitude spread. For the 28 X-ray YSOs with MC09 counterparts, our SED-based disc classification agrees with that of MC09 for all but one source (Section 3.3).

Spitzer-MIPS data are also available (PID 58; PI: Rieke). The use of the MIPS data in this work could potentially lead to revised disc classes for some of the sources – from discless classified by shorter wavelengths to transition discs (TDs), systems with inner disc holes. However, due to the reduced spatial resolution and sensitivity of the MIPS data, such a classification would be biased towards brighter, less crowded objects located mainly outside the globule (the region with the brightest diffuse emission). For simplicity, in this work, we prefer to omit the usage of the MIPS data and to classify any TD candidate as discless (Section 3.3). This should not affect the goals of this paper, identification and characterization of triggered stellar populations.

2.3 FLWO and Calar Alto data

The optical observations of Trumpler 37 and IC 1396A and their data analyses are described in detail by Sicilia-Aguilar et al. (2004), SA05 and Sicilia-Aguilar, Henning & Hartmann (2010).

The UVR_CI_C observations were carried on with the 1.2-m telescope at FLWO, using the 4Shooter CCD array, between 2000 September and 2002 September (Sicilia-Aguilar et al. 2004; SA05). 4Shooter is an array of four CCDs, covering a square of 25 arcmin on the side. Two 4Shooter fields were taken to cover an ∼45 × 25 arcmin^2 area centred on HD 206267. The FLWO fields contain the whole ACIS field, except for a small gap in between the four CCDs of 4Shooter. All but a few *Chandra* stars were observed in 2000 September.

The UVR_JI_J observations of Trumpler 37/IC 1396A were obtained in service mode during three nights in 2007 June 9–11, using the wide-field camera LAICA mounted on the 3.5-m telescope in Calar Alto, Spain (Sicilia-Aguilar et al. 2010). LAICA is a 2 × 2 mosaic of four CCDs, each covering a 15.3 × 15.3 arcmin^2 field of view (FOV) with a large gap of 15.3 × 15.3 arcmin^2 in between. The project combines four LAICA pointings covering an ∼45 × 45 arcmin^2 area around HD 206267, including nearly the entire ACIS field.

After applying standard procedures for bias and flat-field corrections, aperture photometry, and zero-point calibration (Sicilia-Aguilar et al. 2004, 2010), we obtain optical photometry for 181 X-ray sources. The resulted VI_C and VI_J photometric measurements are given in Table 2.

3 IR AND OPTICAL COUNTERPARTS TO X-RAY SOURCES

3.1 Identifications

Positions of our X-ray sources were compared with source positions from the three optical catalogues (SA05/FLWO, B11 and LAICA), the near-IR (NIR) 2MASS catalogue, and the two MIR *Spitzer* catalogues (MC09 and our custom catalogue from Section 2.2).

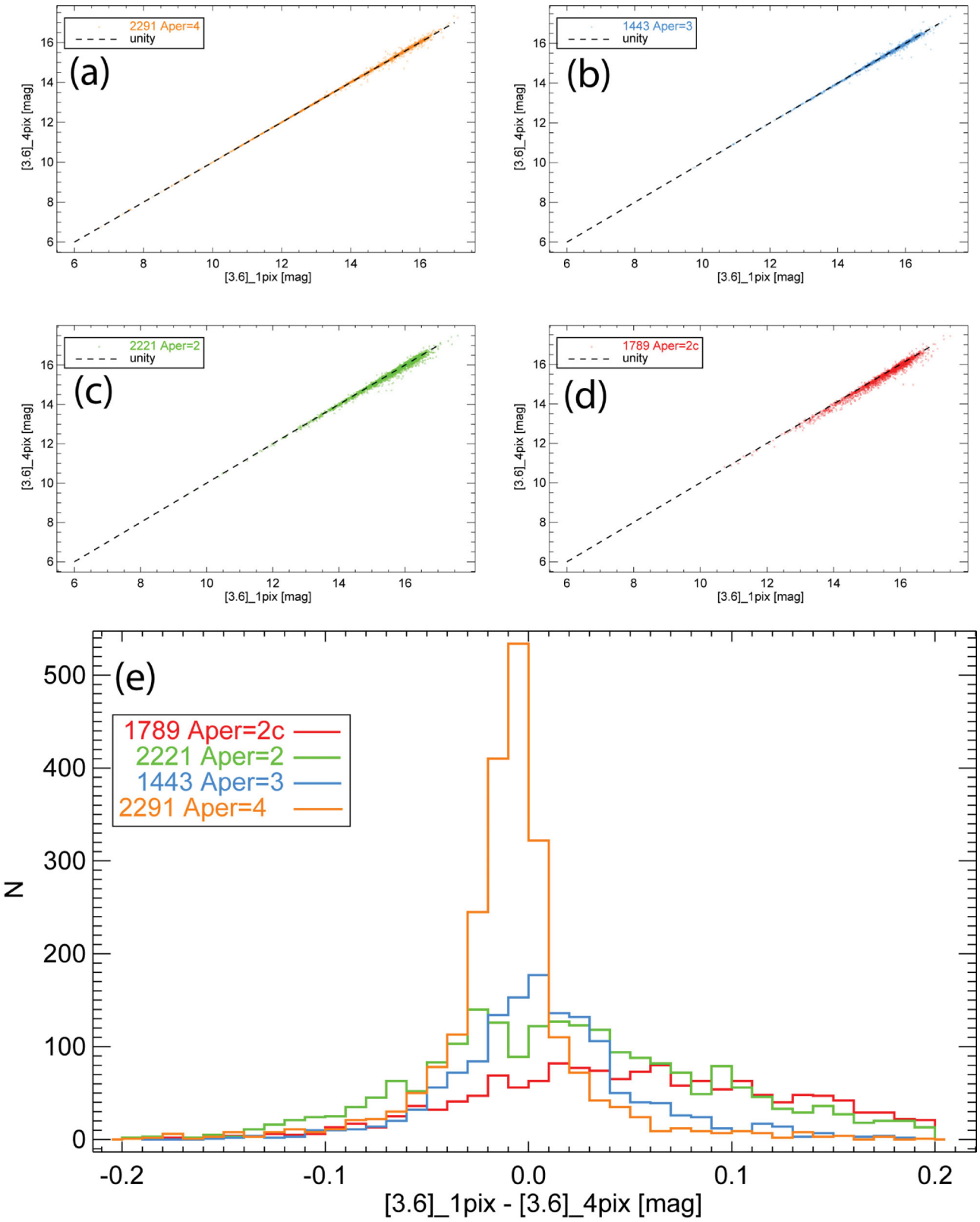

Figure 2. Entire IRAC source sample ([3.6] band). The photometry from 4-pixel-wide background annuli versus the photometry from 1-pixel-wide background annuli. The top four panels show the photometric measurements for the source samples with different source extraction apertures: 4 pixel (orange), 3 pixel (blue), 2 pixel (green) and 2 pixel with possible contaminating flux from a neighbouring source of >10 per cent (red). The bottom panel is a histogram representation of the photometric differences for all four source samples with different source extraction apertures. The median, mean and standard deviation of the magnitude differences are 0.069, 0.094 and 0.133 mag for the '2c' extractions; 0.02, 0.034 and 0.099 mag for the 2-pixel extractions; 0.007, 0.011 and 0.077 mag for the 3-pixel extractions; and −0.008, −0.008 and 0.06 mag for the 4-pixel extractions, respectively.

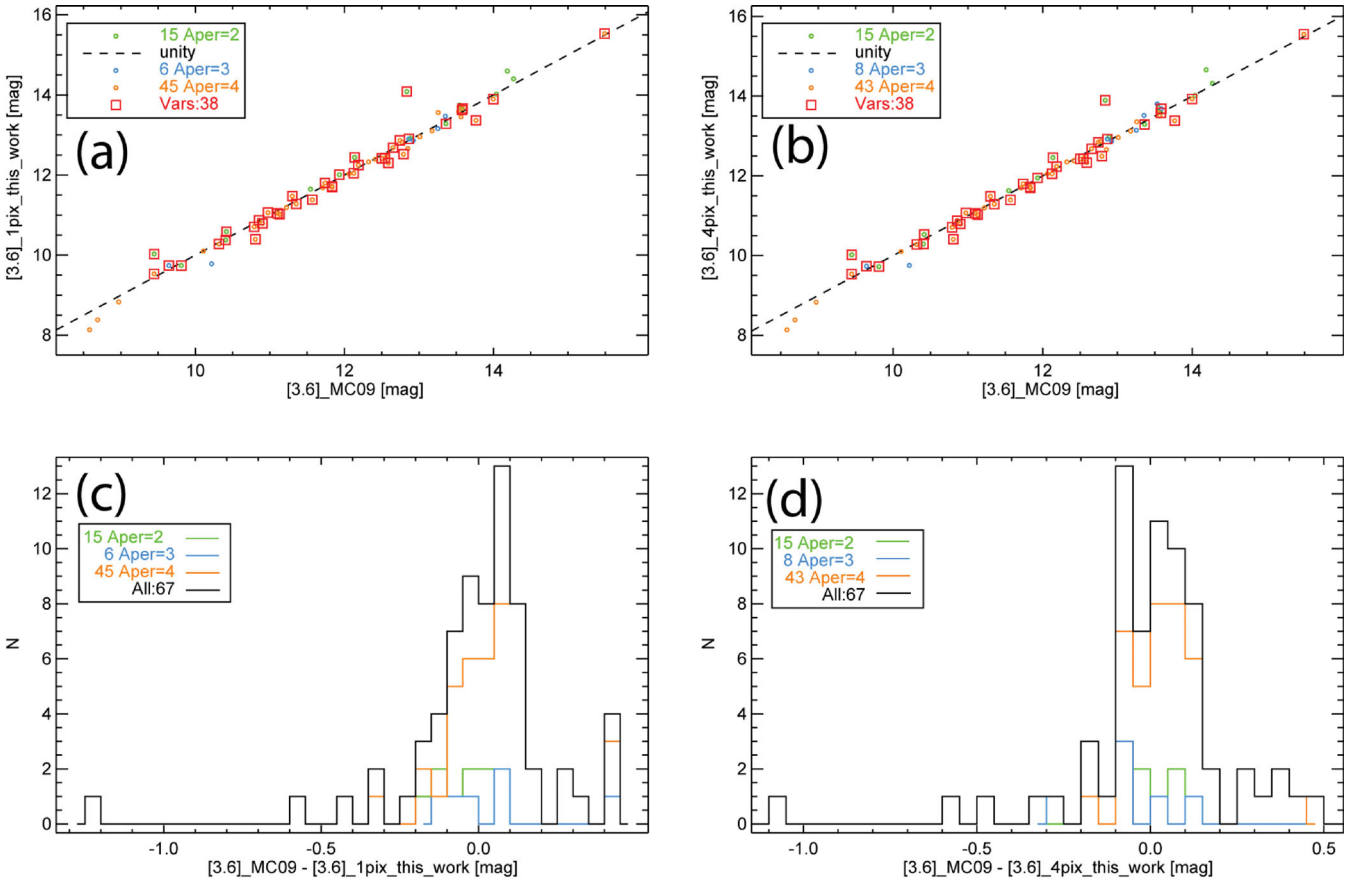

Figure 3. Photometry comparison with the time-averaged measurements of MC09 ([3.6] band). The left-hand (right-hand) panels present the photometric measurements for our 1-pixel (4-pixel) background methods versus MC09 photometry. The top and bottom panels give a scatter plot and a histogram version, respectively. The source samples are colour-coded according to our choice of different source extraction apertures: 4 pixel (orange), 3 pixel (blue) and 2 pixel (green). The MIR-variable sources from MC09 are additionally marked by the red squares. In panel (c), the median, mean and standard deviation of the magnitude differences are: −0.102, −0.207 and 0.341 mag for the 2-pixel extractions; 0.062, 0.057 and 0.203 mag for the 3-pixel extractions; 0.056, 0.064 and 0.153 mag for the 4-pixel extractions; and 0.026, 0.003 and 0.237 mag for the entire sample. In panel (d), the median, mean and standard deviation of the magnitude differences are: −0.082, −0.176 and 0.316 mag for the 2-pixel extractions; −0.058, −0.007 and 0.224 mag for the 3-pixel extractions; 0.056, 0.07 and 0.141 mag for the 4-pixel extractions; and 0.024, 0.006 and 0.222 mag for the entire sample, respectively.

The SA05, B11, LAICA and 2MASS catalogues cover the full ACIS field. Our custom MIR catalogue overlaps 93 per cent of the ACIS field omitting its north-western and south-western edges. The MC09 catalogue covers the inner region of the ACIS field near/inside the globule; this amounts to ∼20 per cent of the ACIS field. The MC09 catalogue includes all disc-bearing stars near/inside the globule reported by Reach et al. (2004) and SA06.

An automated cross-correlation between the *Chandra* source positions and optical–IR source positions was made using a search radius of 2 arcsec within ∼6 arcmin of the ACIS field centre, and a search radius of 3.5 arcsec in the outer regions of the ACIS field where X-ray source positions are more uncertain due to the deterioration of the *Chandra* telescope PSF. This was followed by a careful visual examination of each source in both bands to remove dubious sources and associations.

Optical FLWO/LAICA (Section 2.3), NIR 2MASS and MIR IRAC (Section 2.2) photometry for X-ray sources is given in Table 2. Individual counterparts from 2MASS, our custom IRAC (Section 2.2), SA05, B11 and MC09 catalogues are given in Table 3.

Chandra detects 27 out of 69 (39 per cent) of the MC09 IR-excess objects and 45 out of 76 (59 per cent) of the B11/SA05 Hα emitters and Li absorbers. Most of the optical YSOs undetected in X-rays are disc-bearing stars. The X-ray detection efficiency of disc-bearing stars is known to be lower than that of discless stars (Getman et al. 2009; Stelzer et al. 2012, and Fig. 5 here). To compensate for this effect, in Section 4 we introduce a catalogue of additional non-*Chandra* IR-excess selected discy stars within the ACIS field and beyond. This allows a recovery of 83 per cent of Hα emitters and Li absorbers. Several optical stars located at the very edge of the ACIS field, where the ACIS sensitivity degrades, remain unrecovered.

3.2 Pre-main-sequence census

X-ray surveys of star-forming regions suffer contamination by extragalactic sources, mainly quasars and other active galactic nuclei (AGNs), which can be seen even through the Galactic plane as faint, absorbed X-ray sources. Additional contamination arises from foreground and background Galactic stars, mainly main-sequence stars and some types of giants (Getman et al. 2011, and references therein).

We perform detailed simulations for extragalactic and Galactic X-ray contamination populations expected in the direction of the IC 1396A ACIS field, (l, b) = (99.°1, +3.°9). The methodology for such simulations is detailed in Getman et al. (2011).

Table 3. Derived properties, stellar identifications, membership and classification. This table is available in its entirety as Supporting Information with the electronic version of the article. A portion is shown here for guidance regarding its form and content. Column 1: X-ray source number. Columns 2 and 3: X-ray net counts and median energy for the full (0.5–8.0) keV band. Columns 4 and 5: X-ray column density, intrinsic luminosity and their errors (summed in quadrature statistical and systematic errors). Luminosities are derived assuming a distance of 870 pc and are given for the full (0.5–8.0) keV band. Columns 6 and 7: age estimates derived from the optical V versus $V - I_C$ and V versus $V - I_J$ colour–magnitude diagrams using PMS models of Siess, Dufour & Forestini (2000) and assuming a constant source extinction for optical PMS candidates of $A_V = 1.56$ mag (SA05; B11). Column 8: apparent SED slope from IRAC photometry with 1σ error. Column 9: number of IRAC bands, from which the SED slope was derived. Column 10: 2MASS identifier. Column 11: source identifier from our analysis of the IRAC data; X-ray sources outside the FOV of the IRAC data analysed here are labelled as 'OutOfIracFOV'. Columns 12–14: stellar counterparts from SA05, B11 and MC09. Column 15: this positional flag indicates if an X-ray source lies projected against the globule ('1') or not ('0'). Column 16: indicates the membership and YSO class: 'EXG' – possible extragalactic contaminant; 'FRG' – possible foreground contaminant or YSO; 'DSK' and 'NOD' – discy and discless YSOs, respectively; 'UNC1' and 'UNC2' – objects of the uncertain class. 'UNC1' are sources with no IR counterparts; these are most likely extragalactic objects but some can be background stars. 'UNC2' have weak registered and unregistered IR counterparts or lie close to bright IR objects; these could be YSOs or field stars or extragalactic objects.

S. No.	NC (counts)	ME (keV)	$\log(N_H)$ (cm^{-2})	$\log(L_X)$ ($erg\,s^{-1}$)	t_{FLWO} (Myr)	t_{LAICA} (Myr)	α_0	Np	2MASS	IRAC	SA05	B11	MC09	Region	Class
(1)	(2)	(3)	(4)	(5)	(6)	(7)	(8)	(9)	(10)	(11)	(12)	(13)	(14)	(15)	(16)
...	...	...	...	...	...	...	...	...	...	...	...	...	...	...	...
164	7.8	1.8	–	–	–	–	-1.36 ± 0.10	4	21364762+5729540	J213647.61+572954.1	–	30	IC1396A-61	1	DSK
165	3.4	2.7	–	–	–	–	–	–	–	–	–	–	–	0	UNC1
166	18.9	4.1	23.04 ± 0.21	30.97 ± 0.24	–	–	-1.15 ± 0.20	4	21364788+5731306	J213647.87+573130.6	–	–	IC1396A-28	1	DSK
167	17.9	1.3	21.60 ± 0.50	29.71 ± 0.23	–	–	-2.43 ± 0.07	3	21364793+5723062	J213647.94+572306.5	–	–	–	0	NOD
168	12.5	1.3	–	–	4.7	2.8	-2.54 ± 0.07	2	21364819+5734020	J213648.19+573401.9	–	–	–	0	NOD
169	59.0	1.1	20.15 ± 0.77	29.92 ± 0.09	–	–	-2.83 ± 0.01	4	21364825+5739185	J213648.25+573918.4	–	–	–	0	FRG
170	11.7	3.1	22.58 ± 0.26	30.61 ± 0.30	–	–	–	–	–	OutOfIracFOV	–	–	–	0	UNC2
171	12.8	1.3	21.60 ± 0.69	29.48 ± 0.25	–	–	-2.25 ± 0.11	3	21364866+5730262	J213648.65+573026.2	–	–	–	1	NOD
172	6.9	1.0	–	–	–	–	–	–	–	–	–	–	–	0	UNC1
173	15.9	2.6	22.41 ± 0.17	30.48 ± 0.25	0.6	0.3	-0.94 ± 0.01	4	21364941+5731220	J213649.42+573122.2	14-141	–	IC1396A-29	1	DSK
174	96.1	1.5	21.78 ± 0.21	30.56 ± 0.16	3.5	3.8	-1.76 ± 0.02	4	21364964+5722270	J213649.65+572227.1	–	–	–	0	DSK
...	...	...	...	...	...	...	...	...	...	...	...	...	...	...	...

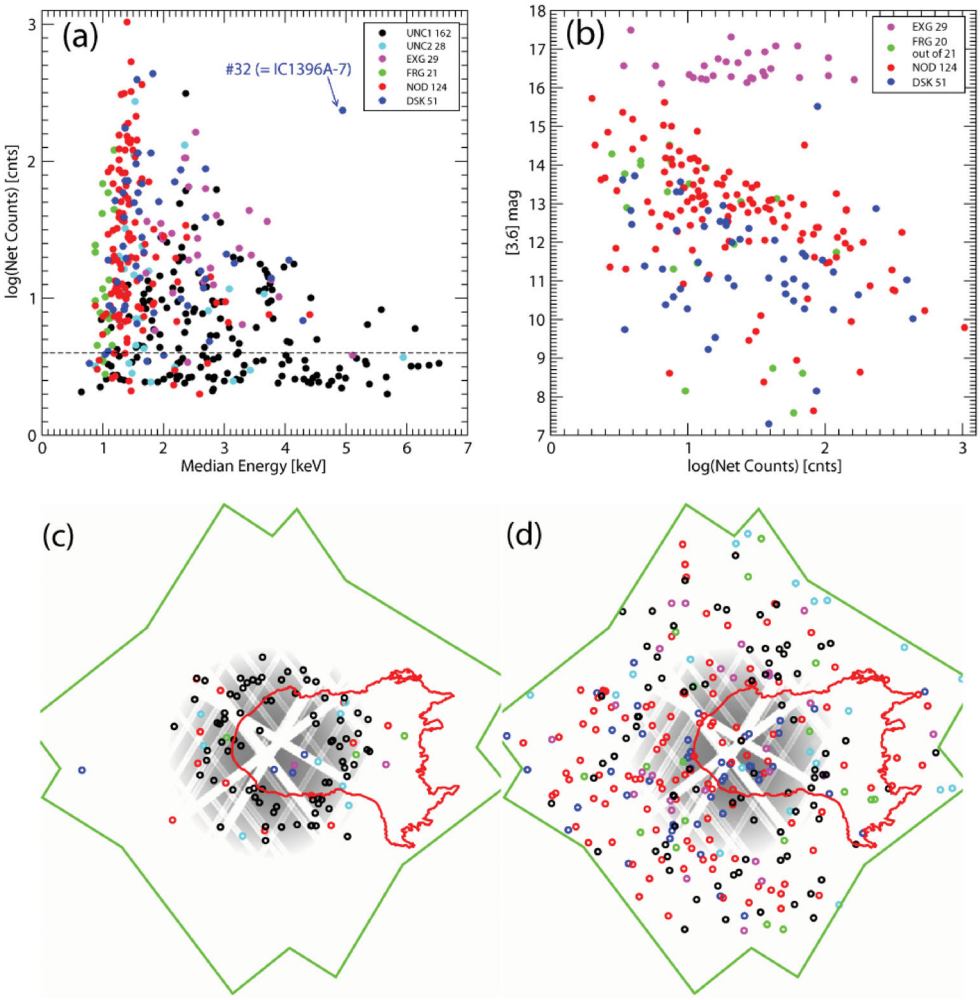

Figure 4. Properties of different classes of X-ray sources. Source classes are colour-coded: the uncertain Class 1 (UNC1), which is largely comprised of extragalactic objects, is in black; the uncertain Class 2 (UNC2), which is possibly a mixture of contaminants and some low-mass YSOs, is in cyan; the EXG class, which is composed of IR–X-ray bright extragalactic objects, is in magenta; the FRG class, which likely contains foreground stars and some YSOs, is in green; and the NOD/DSK classes are composed of young discless/discy members shown in red/blue. Panel (a): X-ray net counts versus X-ray median energy. The dashed line marks the 4 net count level. One of the most reddest Class I protostars found within the globule (*Chandra* source #32 = IC1396A-7) is labelled. Panel (b): 3.6-μm-band magnitude versus X-ray net counts. Panels (c) and (d): spatial distribution of different classes of X-ray sources superposed on the *Chandra* exposure map shown in inverted colours with logarithmic scales. The distributions are stratified by X-ray net counts, NC <4 counts (panel c) and NC >4 counts (panel d). The green polygon outlines the *Chandra* FOV. The red contour demarcates the globule, tracing 8.0 μm emission from hot dust and polycyclic aromatic hydrocarbons (PAHs).

The simulations take into consideration a variety of factors involving a Galactic population synthesis model (Robin et al. 2003), stellar (AGN) X-ray luminosity (flux) functions, *Chandra* telescope response, source detection methodology, and possible spatial variations in the X-ray background and absorption through molecular clouds. For the IC 1396A cloud, we construct its extinction map based on dust reddening of 2MASS sources excluding possible foreground sources, all previously known YSOs, and 2MASS sources with X-ray counterparts (for detailed methodology, see appendix B in Schneider et al. 2011). The derived extinction varies from $A_V <$ 2 mag outside the globule to $3 \lesssim A_V \lesssim 12$ mag through the head of the main globule (behind Rim A) and along the edge of the SFO 36 cloudlet adjacent to Rim Aa (Fig. 1). Our simulations predict that ∼20–30 foreground X-ray stars with X-ray median energies of ME $\lesssim$ 1 keV, ∼20–30 background stars with 1 < ME < 2 keV and ∼110–150 extragalactic objects with ME > 2 keV are present in the ACIS field.

Based on the presence/absence of IR counterparts, source spatial distributions, X-ray counts, X-ray median energies (surrogates for X-ray absorption), and the predicted number of contaminants, the X-ray objects detected in our *Chandra* observation can be separated into the following source classes (see Table 3 and Fig. 4):

(A) Bright extragalactic objects ('EXG').
(B) Uncertain Class 1 (labelled as 'UNC1') mostly composed of faint extragalactic objects.
(C) Uncertain Class 2 ('UNC2'), which is possibly a mixture of contaminants and some low-mass YSOs.
(D) A mixture of foreground stars and possibly some YSOs ('FRG').
(E) Discless and discy young members of the region ('NOD' and 'DSK').

The 29 hard X-ray sources (ME $\gtrsim$ 2 keV; magenta in Fig. 4a) from the class 'EXG' lack 2MASS but have dim MIR counterparts

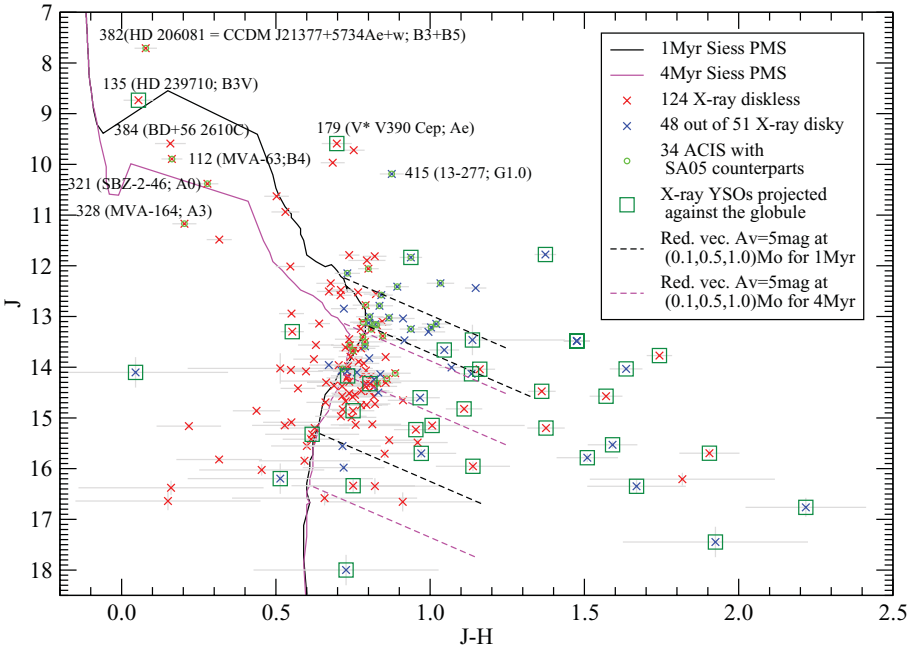

Figure 5. NIR colour–magnitude diagram for all *Chandra* YSOs with available NIR photometry. Discless and disky X-ray stars are marked as the red and blue ×, respectively. Sources projected against the globule are further outlined by green □. X-ray sources with known optical counterparts from SA05 are additionally marked by green ○. 1- and 4-Myr PMS isochrones from Siess et al. (2000) at an 870 pc distance are shown as the solid black and magenta lines, respectively. Reddening vectors of $A_V = 5$ mag for various masses are indicated by the dashed lines. Some previously known intermediate- and high-mass stars are labelled.

([3.6] > 16 mag, [4.5] > 14.5 mag). These are most likely bright extragalactic objects, because they are clear outliers from the stellar locus on the [3.6] versus X-ray net count diagram (Fig. 4b), and their [3.6] and [4.5] magnitudes and X-ray fluxes are fully consistent with those of the *Chandra–Spitzer* AGN sample from the Serendipitous Extragalactic X-ray Source Identification programme (Eckart et al. 2010).

The class 'UNC1' is composed of 162 X-ray sources. We believe that most of these sources are extragalactic objects because they lack IR counterparts, are generally X-ray faint and hard (NC < 4–10 counts and ME $\gtrsim$ 2 keV; Fig. 4a), and their number is comparable to the number of simulated AGNs. Their spatial distribution is also similar to that of the simulated extragalactic objects: the weakest X-ray sources are concentrated towards the central part of the ACIS field, while brighter sources are uniformly distributed across the field (black points in Figs 4c and d). The greater density of very weak X-ray sources on-axis than off-axis is due to the variation in detection completeness with off-axis angle (Broos et al. 2011). The detected X-ray YSOs are much less prone to such an effect because only a handful of them are very weak sources (red and blue points in Fig. 4).

The 28 objects of the class 'UNC2' do not have catalogued IR counterparts, but our visual inspection of the 2MASS and *Spitzer*-IRAC images suggests that some might have very dim uncatalogued counterparts and some lie near bright IR objects. We suggest that this class is a mixture of heterogeneous contaminants and low-mass YSOs.

The remaining X-ray sources with IR counterparts are further divided into 21 possible foreground stars (class 'FRG') and 175 likely YSO members of the region (classes 'NOD' and 'DSK'). The 'FRG' class is composed of stars with low median energies and NIR colours (green in Fig. 4a and Fig. 8a) that are not listed in the optical catalogue of young stars from SA05.

The application of the MIR source classification scheme of Gutermuth et al. (2009) to the X-ray YSO sample yields zero extragalactic candidates. The scheme cannot be applied to the 'EXG', 'UNC1' and 'UNC2' objects, since many of them lack MIR counterparts and all lack [5.8]- and [8.0]-band magnitudes.

Only the 175 likely YSO members (classes 'NOD' and 'DSK') are used in our analyses of the IC 1396A stellar population. In Section 3.3, these sources are further separated into 124 discless and 51 disky X-ray YSOs. The J versus $J - H$ colour–magnitude diagram in Fig. 5 shows that the X-ray catalogue is sensitive to discless and disky stars down to $J \gtrsim 15$ mag and $J \gtrsim 14$ mag, respectively. X-ray YSOs outside the globule have typical source extinctions of $A_V < 2$ mag, while inside the globule stars can be subject to higher extinction of up to $A_V = 7$–10 mag. The optical catalogue of SA05 within the ACIS field (green ○) is not sensitive to stars with $J > 14$ mag or highly absorbed stars. Fig. 6 shows that at $J \gtrsim 14$ mag the X-ray disky sample is well complemented by the MC09 catalogue of disky stars near and inside the globule as well as our custom IRAC catalogue of disky stars outside the globule (Section 4).

In the ACIS field, previous studies had located 76 Hα emitters and Li absorbers (SA05; B11) and/or 69 MIR excess stars (MC09) representing Class I/II YSOs. The *Chandra* source list (Tables 1–3) includes 61 of these previously known members, and discovers 114 new mostly discless members.[5]

[5] Notice in Fig. 4(a) unusually hard and bright emission from one of the reddest Class I protostars in the cloud, *Chandra* source #32 (MC09 source IC1396A-7; source ε from Reach et al. 2004). Detailed X-ray spectral and variability analyses from IC1396A-7 are out of the scope of this paper and will be presented elsewhere.

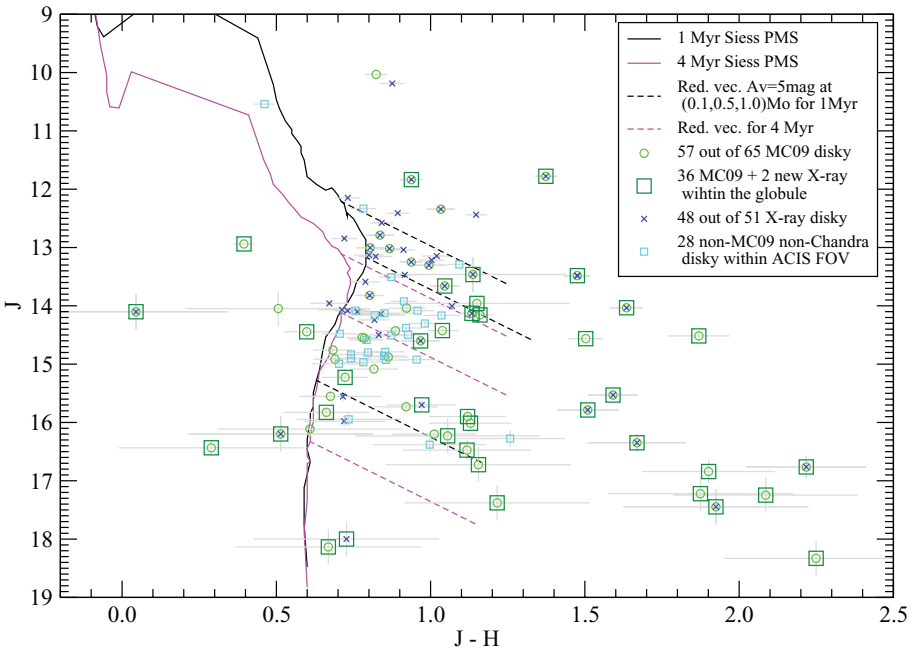

Figure 6. NIR colour–magnitude diagram for all *Chandra*+*Spitzer* discy stars with available NIR photometry identified within the ACIS field. X-ray stars are marked by blue ×. Discy stars from MC09 are marked by green ○. Additional non-*Chandra* and non-MC09 discy stars (from Section 4) within the ACIS field are marked by cyan □. Stars projected against the globule are further outlined by green □. 1- and 4-Myr PMS isochrones from Siess et al. (2000) at an 870 pc distance are shown as the solid black and magenta lines, respectively. Reddening vectors of $A_V = 5$ mag for various masses are indicated by the dashed lines.

3.3 Pre-main-sequence disc classification of X-ray stars

We base the evolutionary classification of X-ray-emitting YSOs in the IC 1396A region on a comparison of their IR SEDs with the SEDs of YSOs in the well-studied IC 348 cluster in the Perseus molecular cloud (Lada et al. 2006). Specifically, we compare the observed IC 1396A SEDs in 2MASS +IRAC IR bands to the (de)reddened median SED templates of IC 348 PMS stellar photospheres. This is our primary classification method and is described in detail in Getman et al. (2009, their section 3). We further confirm these classifications through calculations of the observed SED slope α_0, and locations in IRAC colour–colour diagrams. Results of our disc classification are given in Table 3.

In the SED-based classification, rough estimates of individual stellar masses of the IC 1396A X-ray YSOs are obtained from the J versus $J - H$ colour–magnitude diagram (Fig. 5) using a set of trial age values (1, 2, 3, 4 and 10 Myr). For each trial age, an IC 348 template SED at the corresponding spectral subclass is assigned to each of the X-ray sources. The IC 348 template is (de)reddened and normalized to match both J- and H-band fluxes of the observed IC 1396A source's SED. The reddening applied to the original IC 348 templates to fit the observed IC 1396A SEDs (ΔA_V in Fig. 7) summed with the median source extinction for the discless YSO sample in IC 348 ($A_V = 1.6$ mag from table 2 in Lada et al. 2006) gives an estimate of the source extinction from the SED fitting, $A_{V,\mathrm{SED}}$. We find that $A_{V,\mathrm{SED}}$ is in a reasonable agreement with the source extinction derived from the J versus $J - H$ colour–magnitude diagram, $A_{V,\mathrm{CMD}}$. For example, for the trial age of 2 Myr the median, mean and standard deviation of the $A_{V,\mathrm{SED}} - A_{V,\mathrm{CMD}}$ difference are -0.1, -0.1 and 0.6 mag, respectively.

Visual examination of deviation of the observed IC 1396A SED from the corresponding matched IC 348 photospheric template allows disc classification of IC 1396A X-ray YSOs. While inferred values for individual stellar masses strongly depend on the choice of age, the final classification discriminating discless and discy stars is not age-sensitive. With regard to the 28 X-ray YSOs with MC09 counterparts, our disc classification agrees with that of MC09 for all but one (*Chandra* source #235 = MC09 source IC1396A-46) source. Discy SEDs for 14 X-ray YSOs that do not have counterparts in any previous stellar catalogue and a disc-free SED for the highly absorbed X-ray YSO #235 are shown in Fig. 7.

We also performed least-squares linear fits to the $\log(\lambda F_\lambda)$ values in the four IRAC wavelength bands to obtain the observed (not dereddened) SED spectral index, α_0. These are tabulated in column 8 of Table 3. As in the case of the X-ray-selected YSOs in the Cepheus star-forming region (Getman et al. 2009, their fig. 6), the distribution of the spectral index for IC 1396A X-ray YSOs has a bimodal shape with peaks at $\alpha_0 \sim -1.2$ and -2.7 corresponding to disc-bearing and discless star samples, respectively (graph is not shown). In agreement with the SED-based classification, all but one discless X-ray star have SED spectral indices of $\alpha_0 < -2.1$, and all discy X-ray stars have indices of $\alpha_0 > -2.1$.

In Fig. 8, we compare the SED-based classifications of X-ray stars with the expected loci of YSO stars in NIR and MIR colour–colour diagrams (e.g. Allen et al. 2004; Megeath et al. 2004; Hartmann et al. 2005). The positions of stars in the colour–colour diagrams are in good agreement with our previous classification of stars – simple colour criteria that discy stars have $[3.6] - [4.5] \gtrsim 0.2$, $[4.5] - [5.8] \gtrsim 0.2$ or $[5.8] - [8.0] \gtrsim 0.2$, select nearly all of the SED-based classified discy stars. A couple of stars with the 3.6 − 4.5 colour near zero and with an excess at longer wavelengths could be TD objects, candidates to have inner holes in their discs rather than being discless.

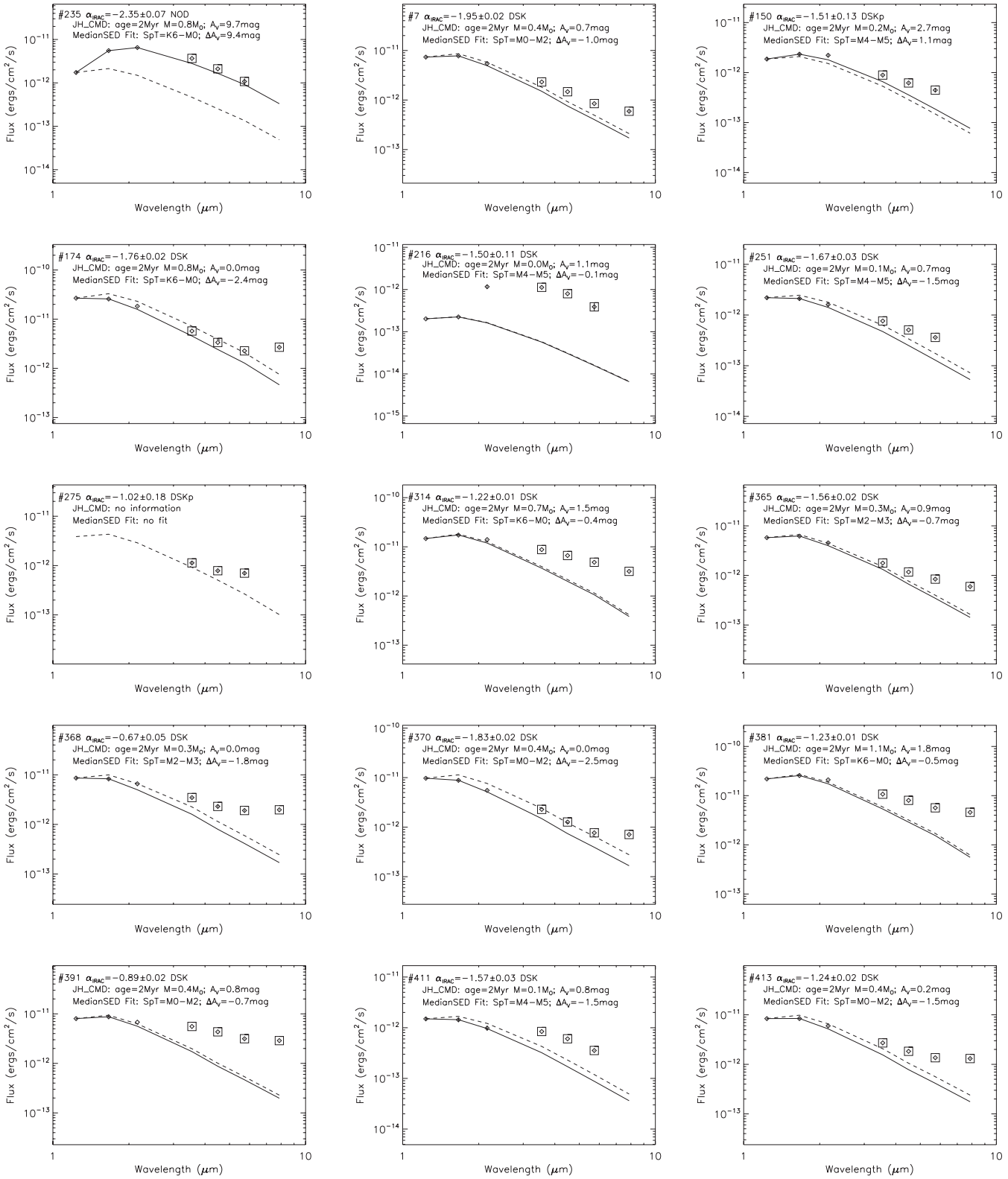

Figure 7. IR SEDs for 14 new X-ray discy stars that are not listed in the previous YSO catalogues. Plus, a disc-free SED for the highly absorbed X-ray source # 235. JHK_s- (diamond) and IRAC-band (square) flux points with usually small errors. The dashed and solid lines give the original and (de)reddened IC 348 median SED from Lada et al. (2006) fitted to the data. The top two lines of the panel legends give information on stellar mass and source extinction estimates derived from the colour–magnitude J versus $J - H$ diagram. The third line gives the spectral class of the corresponding IC 348 median SED template from Lada et al. (2006) and reddening applied to the original template SED to fit the observed IC 1396A source SED.

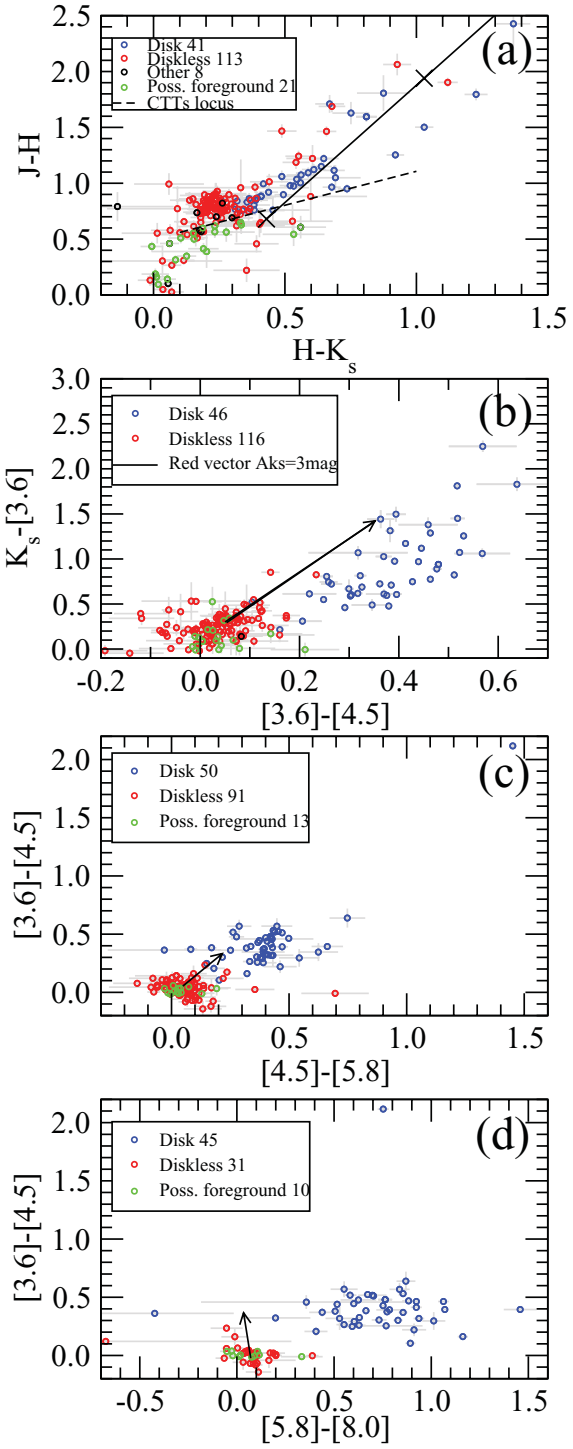

Figure 8. IR colour–colour diagrams of X-ray sources. For all panels, YSO disc-free (Class III) stars with available IR photometry information are in red, YSO discy (Classes I and II) stars are in blue, possible foreground stars unrelated to the region are in green. In panels (b)–(d) the reddening vectors show $A_K \sim 2$ mag using the extinction law from Flaherty et al. (2007). Panel (a): $J - H$ versus $H - K_s$. The dashed line indicates the classical T Tauri star locus (Meyer, Calvet & Hillenbrand 1997). The solid line is a reddening vector marked at intervals of $A_V = 10$ mag. Panel (b): K_s − [3.6] versus [3.6] − [4.5]. Panel (c): [3.6] − [4.5] versus [4.5] − [5.8]. Panel (d): [3.6] − [4.5] versus [5.8] − [8.0].

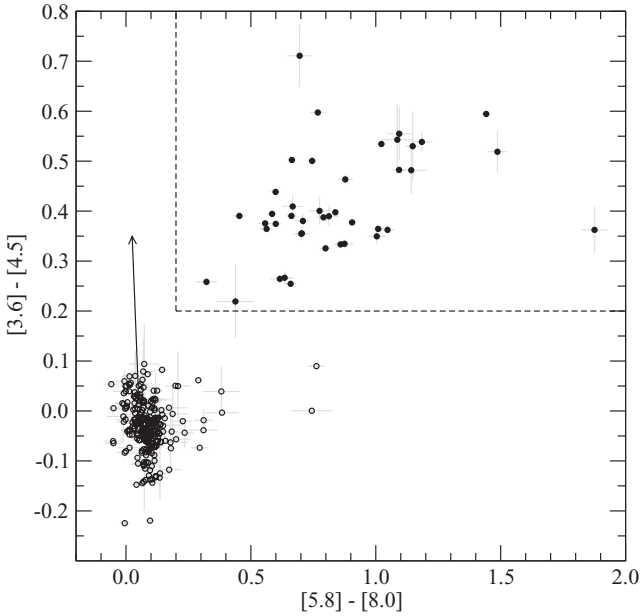

Figure 9. IR colour–colour diagram for non-*Chandra* sources with reliable photometry identified through the analysis of *Spitzer*-IRAC data in this work (Section 4). Classification criteria for selecting discy YSOs, [3.6] − [4.5] $\gtrsim$ 0.2 mag and [5.8] − [8.0] $\gtrsim$ 0.2 mag, are shown by the dashed lines. 42 non-*Chandra* YSOs additional to the discy stars from MC09 are identified (filled circles). The reddening vector shows $A_K \sim 2$ mag using the extinction law from Flaherty et al. (2007).

4 NON-*Chandra* IR-EXCESS MEMBERS

For a given mass, the X-ray detection efficiency of Class II stars is somewhat lower than that of Class III stars (Getman et al. 2009; Stelzer et al. 2012, and Fig. 5 here). To compensate for this effect, this section presents additional non-*Chandra* IR-excess-selected discy stars. The MIR catalogue from MC09 provides an excellent (Section 7.4) selection of discy members near/inside the globule. The catalogue also includes all discy stars near/inside the globule reported by Reach et al. (2004) and SA06. However, MC09 covers only one-fifth of the ACIS field. Thus, we use the results from our *Spitzer*-IRAC data analysis (Section 2.2) to produce an additional sample of non-*Chandra* discy stars for the remaining ACIS field and beyond.

Our IRAC data analysis finds 292 sources not detected by *Chandra* and not published by MC09, with photometric errors < 0.1 mag in all four IRAC bands. Fig. 9 shows the [3.6] − [4.5] versus [5.8] − [8.0] diagram for these sources. Using the IR colour–colour classification criteria presented in Section 3.3, we identify 42 (out of 292) IR-excess stellar candidates. According to the classification scheme of Gutermuth et al. (2009), only one of these sources, source # 29, could be an extragalactic contaminant. Since the IC 1396 region is in the outer Galaxy, we do not expect the sample to be contaminated by asymptotic giant branch or classical Be stars.

Table 4 reports their NIR and MIR magnitudes, apparent SED slope from IRAC photometry, a flag indicating if a source lies within the ACIS field, and stellar counterparts from SA05 and B11. Out of 42 stars, 20 (without SA05 and B11 counterparts) are newly discovered members with 15 of them found within the ACIS field. IR SEDs for these 15 sources are given in Fig. 10. They deviate from photospheric SEDs at wavelengths longer than at least 3.6 μm. As expected, the majority of these new non-*Chandra* discy YSOs are

Table 4. Non-*Chandra* discy stars additional to MC09 stars. Column 1: source number for non-*Chandra* IR-excess sources found in our IRAC data analysis. These sources are located around the globule and are complementary to the IR-excess sources in/near the globule catalogued by MC09. Columns 2 and 3: IRAC right ascension and declination for epoch J2000.0 in degrees. Columns 4–7: 2MASS JHK_s magnitudes, and 2MASS photometry quality and confusion-contamination flag. Columns 8–12: IRAC magnitudes and the aperture flag derived in this work. The flag gives photometric apertures and the level of source contamination from nearby sources and nebular IR emission: 2-pixel (1.73 arcsec), 3-pixel (2.6 arcsec) and 4-pixel (3.46 arcsec) apertures with contaminating flux from a neighbouring source of no more than 10, 5 and 5 per cent in the [3.6] band, respectively. Column 13: apparent SED slope from IRAC photometry with 1σ error. Column 14: a positional flag indicating if a source lies within the ACIS FOV ('1') or not ('0'). Columns 15 and 16: stellar counterparts from B11 and SA05.

S. No.	RA	Dec.	J	H	K_s	F1	[3.6]	[4.5]	[5.8]	[8.0]	F2	α_0	F3	B11	SA05
	(°)	(°)	(mag)	(mag)	(mag)		(mag)	(mag)	(mag)	(mag)					
(1)	(2)	(3)	(4)	(5)	(6)	(7)	(8)	(9)	(10)	(11)	(12)	(13)	(14)	(15)	(16)
1	323.880500	57.524333	14.53 ± ···	13.63 ± 0.05	13.22 ± 0.04	UAA0c0	12.41 ± 0.01	12.15 ± 0.01	12.06 ± 0.02	11.73 ± 0.04	4	−2.04 ± 0.02	0	19	–
2	323.887000	57.533194	14.64 ± 0.04	13.81 ± 0.04	13.51 ± 0.04	AAA000	13.00 ± 0.01	12.64 ± 0.00	12.16 ± 0.01	11.11 ± 0.02	4	−1.09 ± 0.02	1	21	–
3	324.243333	57.650250	16.48 ± 0.15	15.40 ± 0.11	14.62 ± 0.09	BBAccc	13.79 ± 0.03	13.23 ± 0.04	12.66 ± 0.04	11.57 ± 0.03	2	−0.27 ± 0.05	1	–	–
4	324.244708	57.646667	14.14 ± 0.03	13.34 ± 0.04	12.97 ± 0.03	AAA000	12.46 ± 0.00	12.21 ± 0.00	11.90 ± 0.01	11.24 ± 0.02	4	−1.71 ± 0.01	1	–	–
5	324.246292	57.651556	13.57 ± 0.02	12.65 ± 0.03	12.26 ± 0.03	AAA000	11.60 ± 0.00	11.12 ± 0.00	10.57 ± 0.01	9.48 ± 0.03	4	−0.84 ± 0.01	1	34	–
6	324.283917	57.604472	14.58 ± 0.04	13.65 ± 0.04	13.27 ± 0.04	AAA000	12.60 ± 0.00	12.21 ± 0.00	11.84 ± 0.01	11.05 ± 0.03	4	−1.30 ± 0.02	1	–	–
7	324.300708	57.457306	13.39 ± 0.03	12.21 ± 0.03	11.52 ± 0.03	AAA000	10.64 ± 0.00	10.25 ± 0.00	9.96 ± 0.01	9.37 ± 0.01	4	−1.42 ± 0.01	1	–	11-2131
8	324.307917	57.457528	14.27 ± 0.04	13.15 ± 0.04	12.40 ± 0.03	AAAc00	11.42 ± 0.01	10.92 ± 0.00	10.52 ± 0.01	9.78 ± 0.01	4	−1.01 ± 0.02	1	40	–
9	324.309125	57.604889	14.58 ± 0.03	13.59 ± 0.04	13.01 ± 0.03	AAA000	11.91 ± 0.00	11.38 ± 0.00	10.95 ± 0.01	9.93 ± 0.02	4	−0.79 ± 0.01	1	–	–
10	324.314375	57.454722	14.46 ± 0.04	13.48 ± 0.04	12.95 ± 0.04	AAA000	12.14 ± 0.01	11.78 ± 0.00	11.42 ± 0.01	10.86 ± 0.03	4	−1.44 ± 0.02	1	–	–
11	324.321458	57.479806	15.02 ± 0.05	14.20 ± 0.05	13.93 ± 0.07	AAA000	13.31 ± 0.01	12.96 ± 0.01	12.55 ± 0.03	11.55 ± 0.02	3	−0.93 ± 0.03	1	42	–
12	324.333417	57.492861	14.88 ± 0.04	14.11 ± 0.06	13.79 ± 0.06	AAA000	13.14 ± 0.01	12.88 ± 0.01	12.58 ± 0.02	11.94 ± 0.03	4	−1.66 ± 0.03	1	–	–
13	324.339625	57.436778	14.23 ± 0.07	13.36 ± 0.07	12.89 ± 0.04	AAAcc0	12.40 ± 0.04	11.91 ± 0.03	11.57 ± 0.06	10.43 ± 0.02	2	−0.51 ± 0.04	1	–	–
14	324.350333	57.403167	14.20 ± 0.07	13.29 ± 0.08	12.82 ± 0.05	AAAccc	11.94 ± 0.04	11.41 ± 0.05	10.84 ± 0.02	9.69 ± 0.02	2	−0.12 ± 0.05	1	44	–
15	324.351917	57.526639	14.54 ± 0.03	13.79 ± 0.05	13.28 ± 0.04	AAA000	12.59 ± 0.00	12.22 ± 0.00	11.88 ± 0.01	10.87 ± 0.02	4	−1.22 ± 0.02	1	–	21372447+5731359
16	324.364167	57.523222	14.38 ± 0.04	13.34 ± 0.04	12.98 ± 0.03	AAAc00	12.27 ± 0.05	12.05 ± 0.06	11.58 ± 0.04	11.15 ± 0.06	2	−1.52 ± 0.08	1	–	–
17	324.370583	57.601222	13.99 ± 0.03	13.03 ± 0.03	12.63 ± 0.03	AAA000	11.86 ± 0.00	11.47 ± 0.00	11.09 ± 0.01	10.43 ± 0.02	4	−1.33 ± 0.01	1	–	14-1017
18	324.392083	57.575333	15.00 ± 0.04	13.98 ± 0.04	13.49 ± 0.04	AAA000	12.64 ± 0.00	12.24 ± 0.00	11.91 ± 0.01	11.45 ± 0.02	4	−1.44 ± 0.02	1	–	–
19	324.398792	57.549556	14.86 ± 0.04	14.02 ± 0.05	13.62 ± 0.06	AAAc00	13.21 ± 0.01	12.81 ± 0.02	12.45 ± 0.04	11.68 ± 0.02	3	−1.11 ± 0.03	1	48	–
20	324.418667	57.575889	14.99 ± 0.05	14.09 ± 0.06	13.77 ± 0.07	AAA0c0	13.13 ± 0.03	12.61 ± 0.03	11.95 ± 0.03	10.47 ± 0.02	2	0.34 ± 0.04	1	–	–
21	324.428667	57.579500	14.96 ± 0.04	14.18 ± 0.05	13.76 ± 0.05	AAAc00	13.15 ± 0.01	12.79 ± 0.01	12.32 ± 0.02	11.62 ± 0.03	4	−1.22 ± 0.03	1	51	–
22	324.428792	57.608750	10.57 ± 0.02	10.10 ± 0.03	9.84 ± 0.02	AAA000	8.95 ± 0.00	8.35 ± 0.00	7.59 ± 0.01	6.15 ± 0.02	4	−0.27 ± 0.01	1	–	–
23	324.442167	57.574444	14.92 ± 0.05	14.03 ± 0.05	13.64 ± 0.06	AAA000	12.92 ± 0.00	12.56 ± 0.00	12.20 ± 0.02	11.50 ± 0.01	4	−1.30 ± 0.02	1	53	–
24	324.445292	57.532278	14.85 ± 0.05	13.95 ± 0.04	13.63 ± 0.05	AAA000	12.88 ± 0.00	12.55 ± 0.00	12.21 ± 0.02	11.35 ± 0.02	4	−1.36 ± 0.02	1	–	–
25	324.449833	57.545083	14.15 ± 0.04	13.14 ± 0.03	12.77 ± 0.04	AAA000	12.03 ± 0.01	11.69 ± 0.01	11.36 ± 0.01	10.49 ± 0.03	4	−1.47 ± 0.02	1	54	–
26	324.452208	57.499667	15.04 ± 0.06	14.31 ± 0.06	14.05 ± 0.07	AAA000	13.19 ± 0.01	12.78 ± 0.02	12.37 ± 0.03	11.71 ± 0.02	3	−1.16 ± 0.03	1	–	–
27	324.452292	57.405056	–	–	–	–	13.68 ± 0.00	13.08 ± 0.00	12.59 ± 0.02	11.82 ± 0.02	4	−0.67 ± 0.02	0	–	–
28	324.453917	57.389111	14.66 ± 0.06	13.68 ± 0.06	13.25 ± 0.05	AAAc00	12.37 ± 0.01	11.98 ± 0.01	11.64 ± 0.02	10.93 ± 0.02	3	−1.28 ± 0.02	0	55	–
29	324.454958	57.464278	16.04 ± 0.12	15.23 ± 0.12	14.30 ± ···	BBUc00	14.26 ± 0.03	13.90 ± 0.03	13.33 ± 0.05	11.45 ± 0.02	3	0.68 ± 0.04	1	–	–
30	324.455958	57.564333	16.39 ± 0.14	15.04 ± 0.10	14.28 ± 0.09	BAA000	13.79 ± 0.03	13.24 ± 0.06	12.57 ± 0.06	11.48 ± 0.03	2	−0.17 ± 0.05	1	–	–
31	324.463292	57.410000	15.48 ± 0.07	14.68 ± 0.10	14.24 ± 0.07	AAA000	13.34 ± 0.01	12.87 ± 0.01	12.37 ± 0.01	11.49 ± 0.03	4	−0.90 ± 0.02	0	–	–
32	324.468958	57.432250	15.21 ± 0.06	14.42 ± 0.07	13.97 ± 0.06	AAA000	13.72 ± 0.01	13.18 ± 0.01	12.56 ± 0.03	11.38 ± 0.03	3	−0.23 ± 0.03	0	–	–
33	324.496833	57.604472	13.32 ± 0.03	12.40 ± 0.03	11.89 ± 0.02	AAA000	11.13 ± 0.00	10.73 ± 0.00	10.36 ± 0.01	9.52 ± 0.01	4	−1.21 ± 0.01	0	57	13-1238
34	324.514542	57.693028	12.50 ± 0.03	11.48 ± 0.03	10.85 ± 0.02	AAA000	9.83 ± 0.00	9.51 ± 0.00	9.24 ± 0.01	8.44 ± 0.02	4	−1.59 ± 0.01	0	–	82-272
35	324.535125	57.446583	10.51 ± 0.03	9.72 ± 0.03	8.77 ± 0.02	AAA000	7.30 ± 0.00	6.80 ± 0.00	6.41 ± 0.01	5.75 ± 0.02	4	−1.03 ± 0.01	0	–	MVA-426
36	324.535625	57.618778	14.31 ± 0.03	13.43 ± 0.03	12.90 ± 0.03	AAA000	11.45 ± 0.00	11.01 ± 0.00	10.78 ± 0.01	10.18 ± 0.02	4	−1.37 ± 0.01	0	58	13-1426
37	324.538667	57.557250	12.39 ± 0.03	11.57 ± 0.03	11.20 ± 0.02	AAA000	10.60 ± 0.00	10.22 ± 0.00	9.85 ± 0.01	8.95 ± 0.01	4	−1.15 ± 0.01	1	–	13-669
38	324.542417	57.452333	15.05 ± 0.08	13.83 ± ···	13.63 ± ···	AUUc00	13.10 ± 0.06	12.39 ± 0.01	12.30 ± 0.04	11.61 ± 0.02	2	−1.49 ± 0.04	0	–	–
39	324.550000	57.416861	14.53 ± 0.05	13.58 ± 0.04	13.32 ± 0.05	AAA000	12.66 ± 0.01	12.40 ± 0.01	12.10 ± 0.02	11.48 ± 0.03	4	−1.71 ± 0.03	0	–	–
40	324.594958	57.671500	14.83 ± 0.04	13.78 ± 0.04	13.35 ± 0.03	AAA000	12.36 ± 0.00	11.98 ± 0.00	11.74 ± 0.01	11.19 ± 0.02	4	−1.52 ± 0.02	0	64	–
41	324.614250	57.518917	12.36 ± 0.04	11.36 ± 0.04	10.77 ± 0.02	AAA000	10.02 ± 0.00	9.65 ± 0.00	9.33 ± 0.01	8.73 ± 0.02	4	−1.44 ± 0.01	0	70	13-236
42	324.616833	57.512889	12.91 ± 0.03	11.98 ± 0.04	11.25 ± 0.05	AAA000	10.19 ± 0.01	9.80 ± 0.02	9.62 ± 0.03	8.81 ± 0.02	3	−1.32 ± 0.03	0	–	13-157

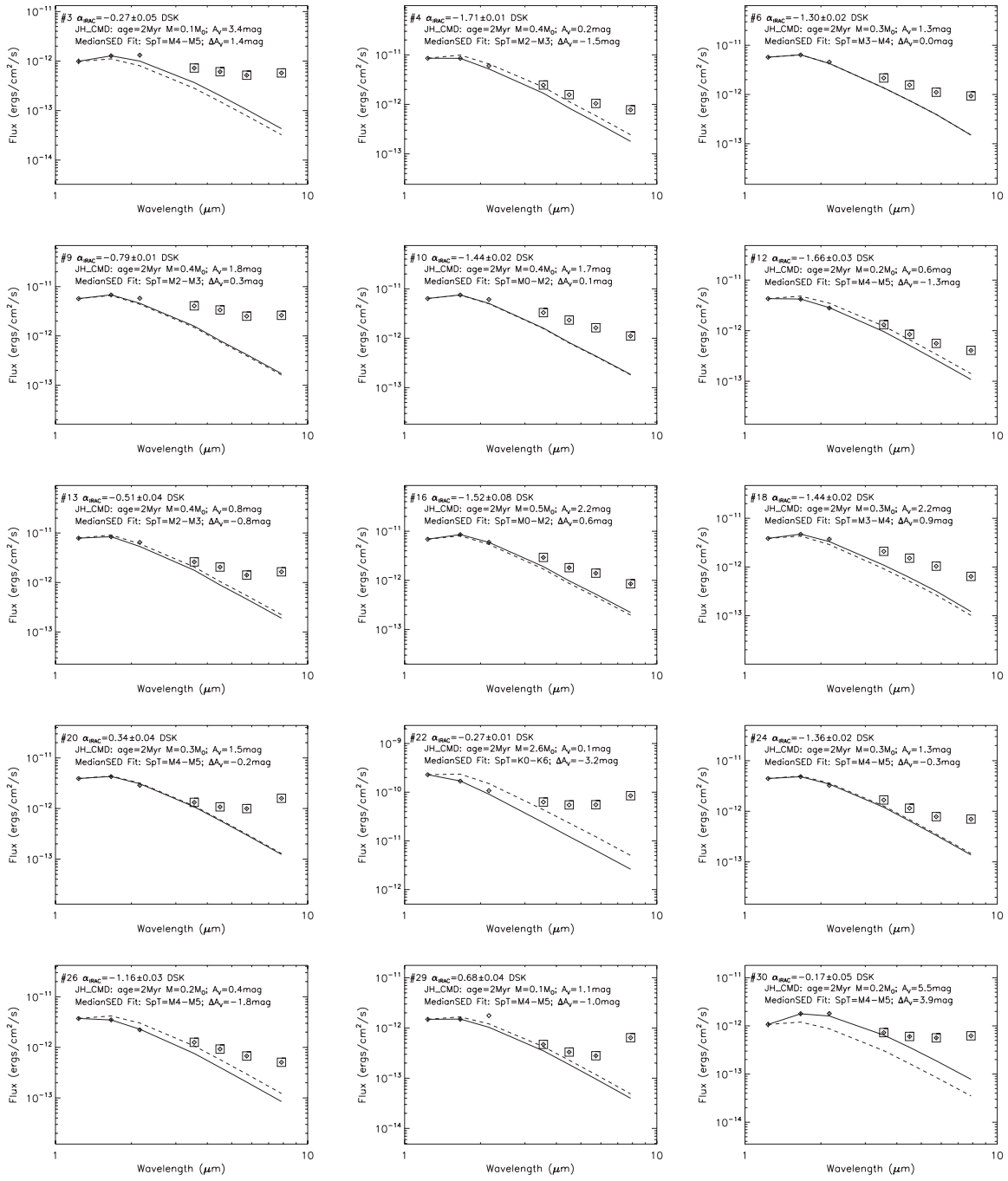

Figure 10. IR SEDs for 15 new non-*Chandra* discy YSOs within the ACIS field that are not in the source catalogues of SA05, MC09 or B11. See Fig. 7 for details.

fainter than the X-ray-selected discy sample (compare cyan □ with blue × in Fig. 6).

5 STELLAR AGE ESTIMATES

Indications of an age gradient among PMS stars, decreasing from the central Trumpler 37 cluster towards the IC 1396A globule, have been reported by SA05 (see their fig. 11) and B11 (their fig. 17). We seek here to confirm this trend and find out if it is statistically significant by taking advantage of the increased stellar sample size near/around the globule and the availability of multi-epoch optical data for many sample members. This requires deriving and comparing in a homogeneous way stellar ages of the combined optical SA05/SA10 and X-ray-selected stellar sample.

It is well known that estimates of individual stellar ages can be very uncertain due to several possible causes such as measurement uncertainty, stellar variability, binarity, different accretional histories, extinction uncertainty, model uncertainty and distance uncertainty (e.g. Baraffe, Chabrier & Gallardo 2009; Soderblom 2010; Preibisch 2012). However, here we are not so much interested in precise ages for individual objects as in the general trends of age distributions and consistent treatment for comparison between different stellar populations. In spite of all the uncertainties, the methods of isochrones and colour–magnitude diagrams often allow

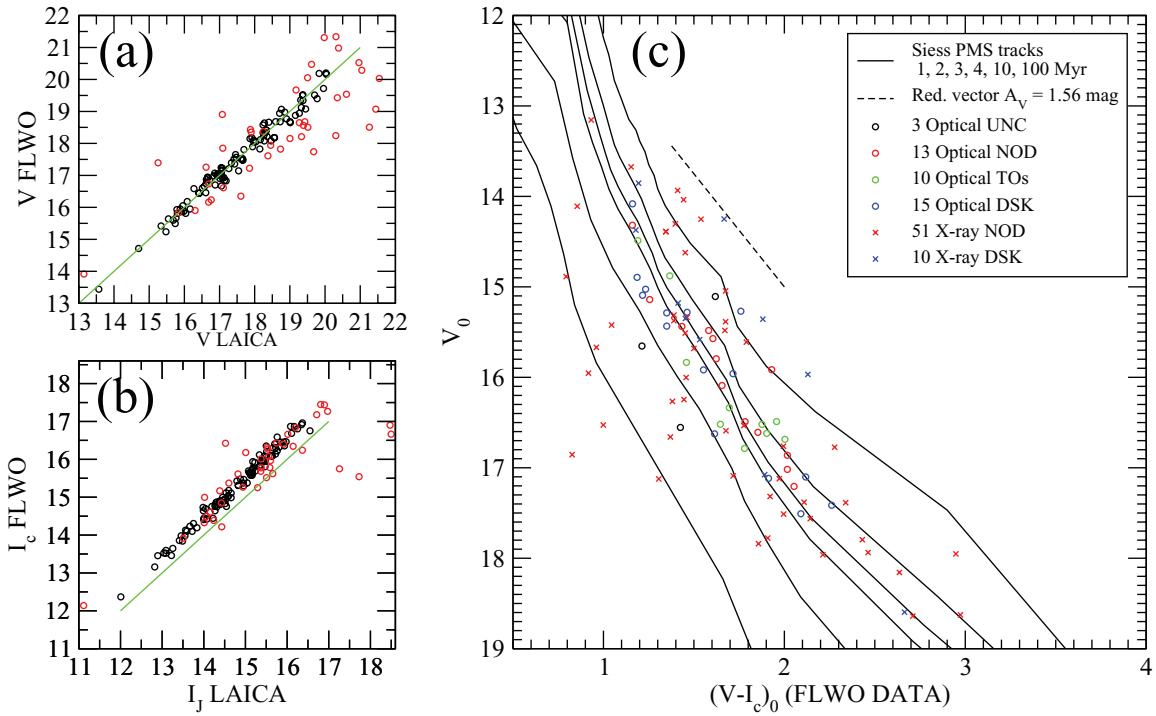

Figure 11. Derivation of ages. Comparison between V-band (panel a) and I-band (panel b) magnitudes for young SA05/SA10 and X-ray stars that have both FLWO and LAICA photometry. The black (red) circles mark 102 (40) stars that have V, I-band magnitudes consistent (inconsistent) between the FLWO and LAICA observations. The unity lines are shown in green. Panel (c): VI_C colour–magnitude diagram for the 102 stars with consistent photometry: 61 X-ray-selected stars (×) and 41 SA05/SA10 stars without X-ray counterparts (○). Colours indicate different disc classes: disc-free (red), disc-bearing (blue), TD objects (green) and uncertain class (black). Magnitudes and colours have been corrected for the average extinction of $\langle A_V \rangle \sim 1.56$ mag (SA05). The black solid lines show PMS isochrones for ages 1, 2, 3, 4, 10, 100 Myr from evolutionary tracks of Siess et al. (2000) assuming a distance of 870 pc (Contreras et al. 2002). The black dashed line shows a reddening vector of $A_V = 1.56$ mag.

discrimination among YSO regions of different characteristic ages (e.g. Burningham et al. 2005; Mayne et al. 2007). The isochronal ages were shown to be in agreement with gravity-related indices (Lawson, Lyo & Bessell 2009). Similar isochronal ages found for binary components in the Taurus–Auriga region are in agreement with the commonly assumed coevality of binary systems (Kraus & Hillenbrand 2009).

First, we clean our source sample to reduce some of the effects that cause age uncertainty. Our initial sample is limited to the stars that have both FLWO and LAICA photometric measurements. These are 89 X-ray stars and 53 SA05–SA10 optical stars without X-ray counterparts. Figs 11(a) and (b) compare their VI-band magnitudes. The systematic difference between the I_C- and I_J-band magnitudes is due to the different photometric systems, FLWO-Cousins versus LAICA-Johnson. The linear transformation $I_C = 0.2954 + 1.0138 \times I_J$ minimizes the differences for all but a few sources with $I_J > 17$ mag. After this I-band correction, large spreads in ΔV and ΔI measurements are seen. The spreads can be mainly attributed to observational uncertainty and stellar variability. To suppress these effects, the sample is truncated to remove sources with $|\Delta V| > 0.4$ mag and $|\Delta I| > 0.4$ mag. The sample is further reduced by removing several sources with possibly high extinction ($J - H > 1.2$ mag corresponding to $A_V > 3$ mag) and/or with known spectral types G–K1. For the latter, their measured ages could be overestimated by incorrect consideration of birth line effects (Hartmann 2003). Our final source sample comprises 102 stars (black points in Figs 11a and b).

The apparent V-band magnitudes and $V - I_C$ colours (and transformed $V - I_J$ colours) are then dereddened by an average extinction of $\langle A_V \rangle = 1.56$ mag (SA05; B11) using the reddening law of $A_I/A_V = 0.6$ (Bessell & Brett 1988). Comparison with the PMS evolutionary tracks of Siess et al. (2000) yields the individual age estimates ($t_{\rm FLWO}$, $t_{\rm LAICA}$) shown in Table 3.

For the final source sample, statistical photometric uncertainties for both V- and I-band magnitudes are <0.04 mag. However, the systematic uncertainty still prevails – only 9 per cent (22 per cent) of the sources have $\Delta V < 0.04$ mag ($\Delta I < 0.04$ mag), but 68 per cent (90 per cent) have $\Delta V < 0.2$ mag ($\Delta I < 0.2$ mag). The FLWO−LAICA age differences quantify the effect of variability on the inferred age estimates: $|t_{\rm FLWO} - t_{\rm LAICA}|/t_{\rm FLWO}$ is better than 10, 20, 30, 40, 50 and 60 per cent for 27, 49, 60, 70, 75 and 80 per cent of the sources, respectively.

Fig. 11(c) shows an optical colour–magnitude diagram for the FLWO data (the LAICA data look similar). There are a dozen diskless stars with inferred ages >10 Myr. Some of them could be members of a possible old distributed population. Half have inferred ages exceeding 100 Myr. This value seems to be unrealistically high considering that the average age for young stars in the region is around 4 Myr (SA05). This may point to variability or to misclassified foreground and background stars. For the analysis below, we limit the sample to stars with a more physically realistic age of <10 Myr.

Fig. 12 shows the spatial distribution of $t < 10$ Myr stars stratified by the ages obtained from the FLWO data; the LAICA data produce similar strata. The region is further divided into two subregions: the east subregion near/around the O6 ionizing star HD 206267 is associated with the central stellar cluster Trumpler 37, while the west subregion near/around the IC 1396A globule is expected to be

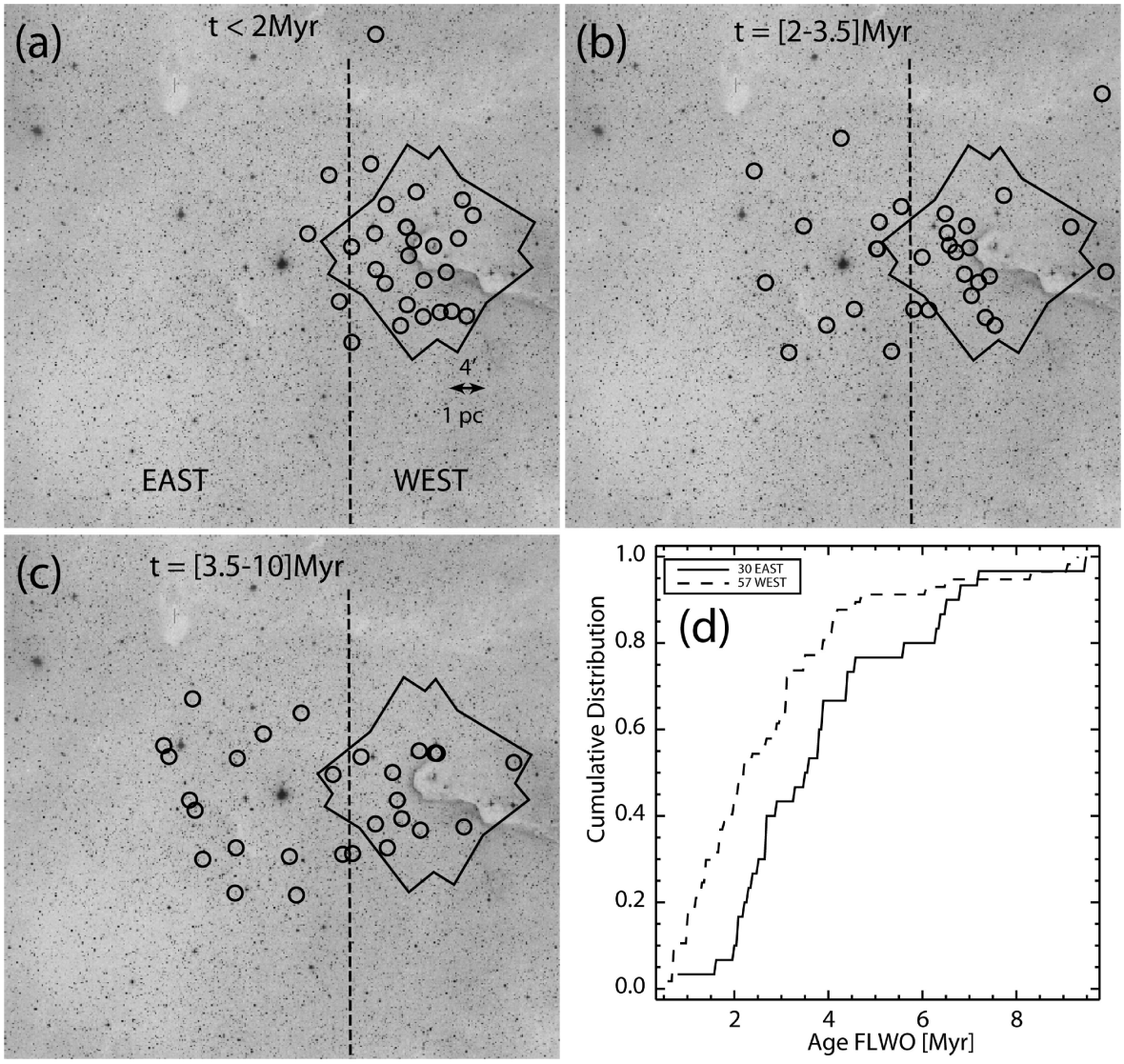

Figure 12. Age analysis for the combined optical SA05 and X-ray-selected young stellar sample. Age-stratified stellar subsamples are shown in different panels: $t < 2$ Myr (panel a), $2 < t < 3.5$ Myr (panel b) and $3.5 < t < 10$ Myr (panel c). The polygon indicates the ACIS FOV. The dashed line at roughly half projected distance between the O6 star HD 206267 and the IC 1396A globule is a demarcation line that divides the region into two subregions, east and west. Panel (d): cumulative distributions of age are compared between the 30 east and 57 west stars with available ages.

associated mainly with stars that have been recently formed in the globule. Our data provide strong evidence that the stars in the east subregion are systematically older than the stars in the west subregion (Fig. 12d). Kolmogorov–Smirnov (K–S) and 'Fisher's exact' tests give small probabilities that the two age samples are drawn from the same distribution.[6] The derived mean/median FLWO (LAICA) ages are 3.9 Myr/3.6 Myr and 2.8 Myr/2.2 Myr (4.4 Myr/4 Myr and 2.7 Myr/1.9 Myr) for the east and west subregions, respectively. These are consistent with the previously reported average age of 4 Myr for the Trumpler 37 cluster (SA05). Typical age estimates for the stars in front of the globule are $t \lesssim 2$–3 Myr. Meanwhile, younger ages ($t \lesssim 1$ Myr) should be assumed for numerous discy objects that are embedded in the globule and lack optical counterparts (Section 7.4).

[6] In the case of the FLWO ages, $P_{KS} = 1.6$ per cent and a 2×2 contingency table with younger/older stars in the east:west region =14/16: 42/15 is consistent with $P_{Fisher} = 1.8$ per cent. In the case of the LAICA ages, $P_{KS} = 0.01$ per cent and a 2×2 contingency table with younger/older stars in the east:west region = 11/18: 45/14 is consistent with $P_{Fisher} = 0.08$ per cent. The derived probabilities are significantly lower than the conventional criterion for statistical significance of $\lesssim$5 per cent (http://en.wikipedia.org/wiki/Statistical_significance). Thus, the null hypothesis that the two samples are drawn from the same age distribution can be confidently rejected.

6 SPATIAL STRUCTURE

In this section, we combine data from different stellar catalogues in order to examine spatial distributions of all known young stars in/around the globule and the neighbouring Trumpler 37 cluster. For the central part of the Trumpler 37 cluster, we utilize optical data from SA05, while for the region in and around the globule we consider the MIR catalogue of MC09, the X-ray catalogue and our additional MIR catalogue from Table 4. The latter three catalogues in turn include discy YSOs from Reach et al. (2004) and SA06 as

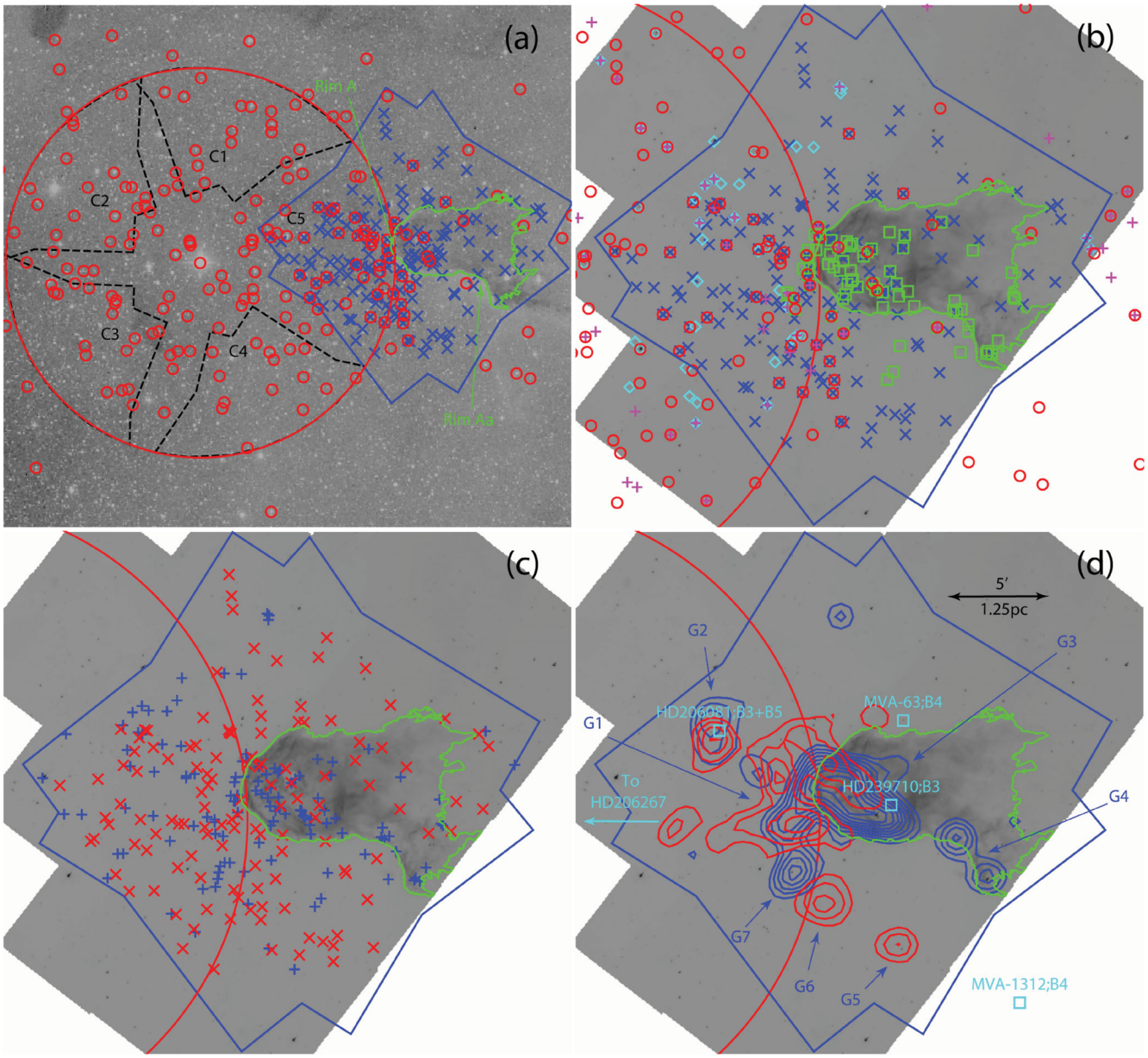

Figure 13. Spatial distribution of known young members of the region overplotted on DSS2-Red (panel a) and *Spitzer*-IRAC 8-μm (panels b–d) images. In all panels, the big red circle outlines the area of the central cluster Trumpler 37 of radius $R = 15$ arcmin centred on the O6 star HD 206267. The blue polygon outlines the ACIS field. The green polygon demarcates the globule, tracing 8.0 μm emission from hot dust and PAHs. Panel (a): positions of young members from the SA05 (red ○) and the X-ray (blue ×) catalogues. 'C1' through 'C5' label five equal-area segments at the edge of the central cluster. Positions of the two optically bright rims in front of the cloud are marked by arrows and labelled in green. Panel (b): positions of all known young members of the region within the ACIS field: optical SA05 (red ○), X-ray selected (blue ×), MIR stars from MC09 (green □), Hα stars from B11 (magenta +), and additional MIR selected stars from this study (cyan ◇). Panel (c): separation on X-ray-selected discless stars (red ×) and discy stars (blue +) combined from MC09 and this work. Panel (d): contour maps of source surface densities from panel (c) smoothed with a Gaussian $\sigma = 1.4$ arcmin. Source density contours are in linear units from 0.75 to 1.5 sources arcmin^{-2} for discless (red), and from 0.75 to 3 sources arcmin^{-2} for discy (blue) stars; both with a step of 0.25 sources arcmin^{-2}. Stellar enhancements above the 1.25 sources arcmin^{-2} level are indicated by arrows and labelled in blue. Known YSOs with spectral type earlier than B6 are marked in cyan. North is up, east is to the left.

well as all Hα stars recently identified within the ACIS field by B11. See Fig. 13 for the spatial distribution of these stars.

6.1 Stellar surface density gradient from the SA05 sample

Here we define the central portion of the Trumpler 37 cluster as as a circular area of radius $R = 15$ arcmin (large red circle in Fig. 13) centred on the O6 star HD 206267 and bordering the head of the IC 1396A globule. We refer to this area hereafter as the R15 area. Nearly the entire area is within the central 4-Shooter field (figs 1 and 9 in SA05), which has a uniform and deep optical exposure. The circular area comprises 150 optical young stars (tables 1, 3 and 5 in SA05). The cluster is not centrally concentrated. For instance, compared to the younger Orion Nebula Cluster (ONC) where the surface stellar density drops by a factor of >25 from the centre to the 2.5 pc radius (Hillenbrand & Hartmann 1998), the density in

Trumpler 37 decreases by only a factor of 2 over a similar parsec scale.

Our goal here is to search for local stellar surface overdensities on the periphery of the R15 area that could be related to TSF in now-dissipated molecular cloudlets. The overlap region between the R15 area and the ACIS field (labelled as 'C5' in Fig. 13a) is especially useful in regards to possible TSF in the originally larger IC 1396A cloud. The periphery of the R15 area is divided by five control equal-area segments labelled as 'C1'–'C5'. From the SA05 master sample, we count 16, 20, 18, 15 and 35 stars in segments C1, C2, C3, C4 and C5, respectively. We thus find that the stellar surface density in the C5 area is two times higher (with statistical significance $P > 99.5$ per cent) than the average density in the remaining periphery area of the central cluster. The ∼17 extra stars could be associated with TSF in the originally larger IC 1396A cloud.

6.2 Increase in the census of YSOs in and around IC 1396A

As X-ray emission from PMS stars is based on enhanced solar-type magnetic reconnection events rather than disc or accretion processes, X-ray selection delivers rich and clean samples of discless stars missed by IR selection (Feigelson 2010). Previous studies have identified 129 YSO members within our ACIS FOV. This study has doubled that census by identifying 130 additional stellar members in our X-ray (Section 3.2) and MIR (Section 4) catalogues (Fig. 13b). 29 members (14 *Chandra* and 15 non-*Chandra*) exhibit an IR excess.

6.3 Stellar surface density gradient from the combined stellar sample

A map of the combined sample of 259 members is shown in Fig. 13(c). They appear clustered rather than uniformly distributed, and the distributions of the discy (blue +) and discless (red ×) stars appear to be offset horizontally from each other. This is more plainly seen in the source surface density maps shown in panel (d), which were constructed using a fixed Gaussian kernel.

Directly in front of the molecular globule, most of the discless and a portion of the discy stars lie in a >3 pc long and ∼0.7 pc wide layer. This result is robust against observation selection effects as the excess of the stars within the layer is seen for both the *Chandra* X-ray-selected disc-free stars and the discy stars that were mainly identified through *Spitzer* IR selection. The position of the layer is also consistent with the positions of the very young optical stars (SA05; B11) and with the excess of the optical stars on the western border of Trumpler 37 that was discussed in Section 6.1.

The layer can be further subdivided into a few stellar groupings: about 30 discy and discless stars along the bright rim and to the east of the globule towards the direction of the major ionizing system HD 206267 (labelled as 'G1'); about 20 discy and discless stars to the north-east of the globule around the B3+B5 high-mass system HD 206081 ('G2'); about 20 stars to the south-east of the globule (the discy 'G6' and the discless 'G7'). Some groupings are discy and others discless, suggesting different ages from distinct RDI events in different cloud cores over millions of years (Section 8.3.2).

Inside the globule, the stellar population is dominated by discy objects, whose spatial distribution is also highly non-uniform and clumpy, with the bulk of the stars lying along the western edge of the globule that faces the ionizing system HD 206267. Two major stellar groupings are seen inside the cloud: a larger group composed of ∼50 Class III/II/I sources at the head of the globule behind bright optical Rim A (group 'G3'); and a smaller group composed of ∼10 sources, mainly Class I protostars, located behind optical Rim Aa in the portion of the cloud named SFO 36 (group 'G4').

6.4 Disc-fraction gradient

The source surface densities of the discless and discy stars lying within the ACIS field inside and in front of the cloud suggest a spatial gradient of apparent disc fraction (Fig. 13d). The highest disc fractions are inside the cloud, behind Rims A ($9/9 = 100$ per cent) and Aa ($35/47 = 75 \pm 6$ per cent).[7] An intermediate disc fraction of $41/85 = 48 \pm 5$ per cent is found in the layer with the enhanced stellar surface density in front of the globule (groups 'G1', 'G2', 'G6' and 'G7' =G1267). Eastward of the layer, towards Trumpler 37, the disc fraction is lowest ($12/34 = 35 \pm 8$ per cent) and is consistent with a recent estimate of the intrinsic disc fraction (39 per cent, Mercer et al. 2009). This disc-fraction gradient within our sample is a tentative finding, for two reasons. First, the gradient is statistically significant across the G1267-globule region, but not across the Trumpler 37–G1267 region.[8] Secondly, the comparison is performed with apparent disc fractions, which are subject to a spatially varying X-ray sensitivity that is suppressed inside the globule.

7 XLFs AND IMFs FOR THE STELLAR POPULATIONS IN THE TRUMPLER 37/IC 1396A REGION

We construct XLFs and IMFs independently for the different projected regions on the sky. The separation into the older Trumpler 37 and younger (likely triggered) IC 1396A stellar populations will be made in Section 8. For stars outside the globule in the ACIS field, two independent analyses are performed: an XLF analysis for purely X-ray selected stars (Section 7.1), and an IMF analysis for the combined X-ray and MIR YSO sample (Section 7.2). The IMF analysis of the optical SA05 YSO sample is employed to measure the total stellar population within the R15 area around HD 206267 (Section 7.3). Finally, the IMF of a stellar sample mainly composed of discy YSOs from MC09 combined with some additional X-ray stars is utilized to estimate the total number of stars inside the globule within the ACIS field (Section 7.4).

7.1 XLF of the stellar population around the globule

Comparison of XLFs between newly studied young stellar clusters like IC 1396A and a well-characterized cluster like the ONC can give insight into any missing population of stars. The assumption of a universal XLF (Feigelson & Getman 2005) has been used in the past to estimate total populations in several young clusters, such as Cep B (Getman et al. 2006), M17 (Broos et al. 2007), NGC 6357 (Wang et al. 2007), NGC 2244 (Wang et al. 2008), NGC 2237 (Wang et al. 2010), W40 (Kuhn et al. 2010), Trumpler

[7] Errors on disc fractions have been estimated using binomial distribution statistics as described by Burgasser et al. (2003).

[8] For the G1267-globule area, a 2 × 2 contingency table with the discy-to-disc-free ratio = 41/44: 35/12 is inconsistent with the null hypothesis of no disc-fraction gradient ($P_{\rm Fisher} = 0.5$ per cent, using Fisher's exact test). However, for the Trumpler 37–G1267 area, a 2 × 2 contingency table with the discy-to-disc-free ratio = 12/22: 41/44 is consistent with the null hypothesis of no disc-fraction gradient ($P_{\rm Fisher} = 23$ per cent).

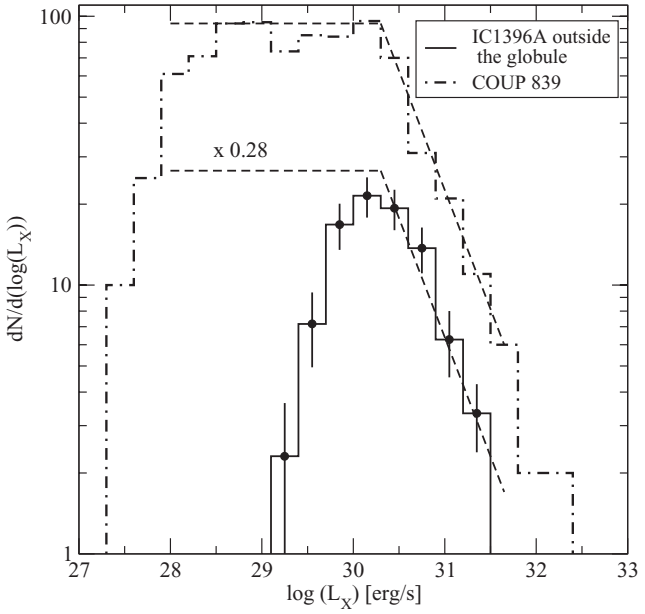

Figure 14. Comparison between XLFs of the ONC and the population of the X-ray-selected YSOs located outside the IC 1396A globule. The dot–dashed histogram shows the COUP unobscured cool sample of 839 stars; the solid histogram is for the sample of 91 X-ray-selected YSOs with available X-ray luminosity information located around the IC 1396A globule. The error bars indicate 68 per cent confidence intervals (1σ) from Monte Carlo simulated distributions as described in the text. The thin dashed lines are added to aid the eye; they are based on the shape of the ONC XLF and scaled downwards to match the IC 1396A XLF.

15 (Wang et al. 2011), Trumpler 16 (Wolk et al. 2011), Sh 2-254/255/256/257/258 (Mucciarelli, Preibisch & Zinnecker 2011) and NGC 1893 (Caramazza et al. 2012). Notice that XLFs are relatively insensitive to age effects; between 0.1 and 10 Myr, only a slight change (roughly 0.3 in $\log L_{\rm X}$) is found in the ONC stellar population (Preibisch & Feigelson 2005; Prisinzano et al. 2008).

For the X-ray-selected young stars related to IC 1396A, X-ray luminosities ($L_{\rm X}$) and absorbing column densities ($N_{\rm H}$) are generated using the non-parametric method XPHOT (Getman et al. 2010). The concept of the method is similar to the long-standing use of colour–magnitude diagrams in optical and IR astronomy, with X-ray median energy replacing colour index and X-ray source counts replacing magnitude. Empirical X-ray spectral templates derived from bright sources from the Chandra Orion Ultradeep Project (COUP; Getman et al. 2005) are further used to translate apparent photometric properties of weak PMS stars into their intrinsic properties. The advantage of the XPHOT method over a traditional parametric spectral modelling (e.g. XSPEC) is that it is more accurate for very faint sources and provides both statistical and systematic (due to the uncertainty in the X-ray model) errors on derived intrinsic fluxes and absorptions. The XPHOT results are given in Table 3.

Fig. 14 shows the XLF for all X-ray-selected YSOs with available $L_{\rm X}$ information that lie outside the IC 1396A globule. The error bars on the XLF were generated from 1000 Monte Carlo simulated XLF distributions with individual X-ray luminosities randomly drawn from Gaussian distributions with the mean equal to the measured source's $\log(L_{\rm X})$ and variances based on the corresponding statistical and systematic errors summed in quadrature. Overplotted is a template XLF for the COUP unobscured population (839 cool ONC stars in Feigelson et al. 2005), which is nearly complete down to $M = 0.1\,{\rm M}_{\odot}$ (section 7.2 in Getman et al. 2006).

The IC 1396A XLF falls quickly below $\log(L_{\rm X}) < 30.0\,{\rm erg\,s^{-1}}$ due to incompleteness, with a conservative value for the completeness limit at around $\log(L_{\rm X}) = 30.5\,{\rm erg\,s^{-1}}$. From the M–$L_{\rm X}$ correlation of Preibisch et al. (2005) and Telleschi et al. (2007) this corresponds to a mass value of $M \simeq 1\,{\rm M}_{\odot}$.[9] Matching the two cluster XLFs in the range $30.5 < \log(L_{\rm X}) < 31.5\,{\rm erg\,s^{-1}}$ requires scaling down the ONC unobscured population by a factor of ∼0.28, yielding a total of ∼235 stars down to $0.1\,{\rm M}_{\odot}$ outside the IC 1396A globule within the ACIS FOV. Notice that the observed weak X-ray sources without available $L_{\rm X}$ information do not affect the results of the analysis because their X-ray luminosities are expected to be below the completeness limit.

7.2 IMF of the stellar population around the globule

In the area outside the globule covered by the ACIS field and all four bands of the IRAC mosaic, we examine the stellar IMF separately for discless and discy stars. To compensate for the effect of higher X-ray detection efficiency of Class III stars, we use the discy stellar sample that is a combination of the *Chandra* and non-*Chandra* IR-excess member young stars (Tables 3 and 4 in this work, and table 2 from MC09) while retaining the discless stellar sample as purely composed of X-ray stars (Table 3).

Approximate stellar mass estimates are obtained based on star locations in the J versus $J - H$ colour–magnitude diagram and theoretical stellar model tracks derived by Baraffe et al. (1998) (for $0.02 \leq M \leq 1.4\,{\rm M}_{\odot}$) and Siess et al. (2000) (for $1.4 \leq M \leq 7.0\,{\rm M}_{\odot}$). These colour–magnitude diagrams are shown in Figs 5 and 6. We are aware of the fact that these mass estimates are subject to significant uncertainties and may be incompatible with individual masses obtained by other methods such as optical spectroscopy (Kuhn et al. 2010, their appendix section). However, here we are not so much interested in exact masses for individual objects as in the general trends of mass distributions and consistent treatment for comparison between different stellar populations.

Typical derived age estimates for the stars in front of the globule are $t \lesssim 2$–3 Myr (Section 5). Fig. 15 shows the IMF of YSOs outside the globule for an assumed age of 2 Myr. The mass distribution within errors follows the shape of the Galactic field IMF with rough mass completeness limits at 0.3–0.4 $\rm M_{\odot}$. The disc fraction obtained by counting discless and disc-bearing stars with masses above the completeness limit is 41 ± 5 per cent. The inferred total number of stars is around 250 stars down to $0.1\,{\rm M}_{\odot}$. Similar results are obtained from the IMF analysis with the assumption of an age of 3 Myr (figure is not shown). The total number of stars (∼250) obtained here from the IMF is consistent with the total (∼235) derived from the age-insensitive XLF analysis (Section 7.1).

7.3 IMF of the central part of Trumpler 37

We estimate the total number of young stars in the central part of Trumpler 37 within the R15 area centred on the O6 star HD 206267 using the optical catalogue of SA05. For the central cluster, we assume the age of ∼4 Myr (SA05, and Section 5 here). As in Section 7.2, stellar mass estimates are derived from the J versus $J - H$ colour–magnitude diagram.

[9] The alternative IMF analysis (Section 7.2) will further show that the inclusion of additional non-*Chandra* Class II members selected by IR excess will push the mass completeness limits for all known YSOs outside the globule down to 0.3–0.4 $\rm M_{\odot}$.

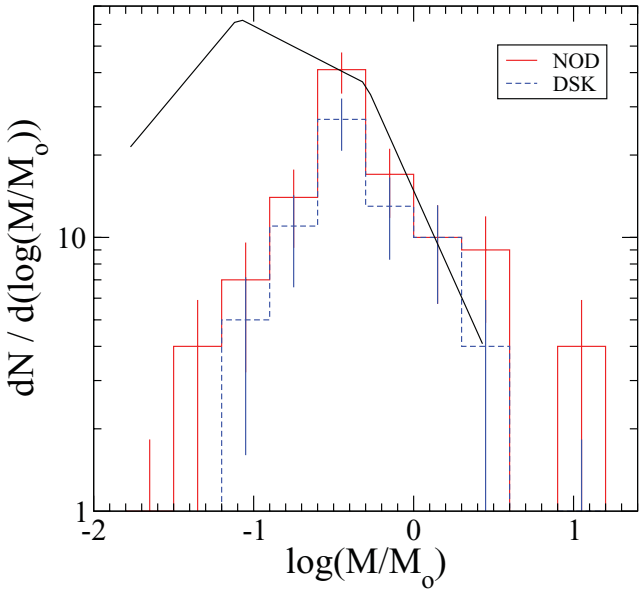

Figure 15. The mass distribution of all known X-ray- and IR-excess-selected YSOs outside the globule within the ACIS FOV, assuming an age of ∼2 Myr. The red and blue histograms are for discless and discy YSOs, respectively. The 1σ Poisson errors (Gehrels 1986) are also shown. The black line represents the scaled version of the Galactic field IMF (Kroupa 2002).

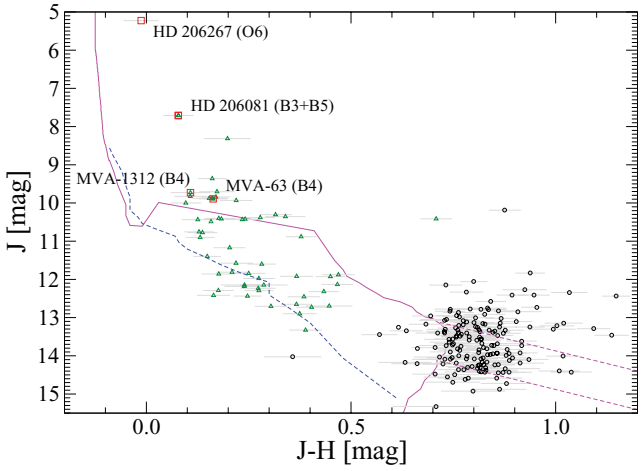

Figure 16. The NIR colour–magnitude diagram for all (inside and outside the ACIS field) optical YSOs from SA05. Low-mass stars are shown as black circles; intermediate- and high-mass stars are shown as green triangles. The unabsorbed zero-age main-sequence and 4-Myr PMS isochrones at an 870 pc distance are shown as the dashed blue and solid magenta lines, respectively. Reddening vectors of $A_V = 5$ mag for masses 0.5 and 1 M$_\odot$ are indicated by the dashed magenta lines. Stars of spectral type earlier than B6 are outlined by red □ and labelled.

Fig. 16 shows that about 20 intermediate-mass YSO candidates lie far to the left-hand side from the 4-Myr isochrone with some of them along the zero-age main-sequence locus. It is unclear if these are members of an old distributed population or older stars unrelated to the region. These stars are excluded from the IMF analysis.

Fig. 17 shows that the mass distribution for the optical stars in the central cluster within errors follows the shape of the Galactic field IMF. The approximate mass completeness limit for the optical sample is 0.8 M$_\odot$. The inferred total number of stars in the R15 area is found to be 480 stars down to 0.1 M$_\odot$. This IMF population and the XLF population from Section 7.1 are consistent in the overlap region between the R15 area and the ACIS field.

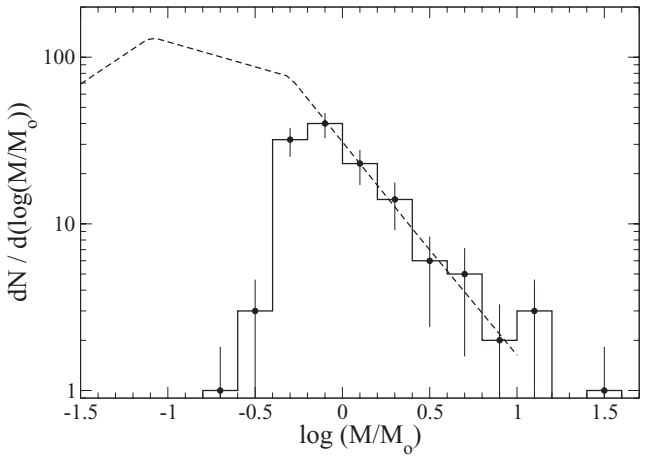

Figure 17. The mass distribution for optical SA05 stars located within the R15 area around the O6 star HD 206267 (solid histogram). The dashed line represents the scaled version of the Galactic field IMF (Kroupa 2002). The 1σ Poisson errors (Gehrels 1986) are also shown.

7.4 Estimate of the stellar population inside the globule

The J versus $J - H$ diagram of X-ray-selected YSOs shown in Fig. 5 suggests that the X-ray detection efficiency of discy stars is lower than that of discless stars. The J versus $J - H$ diagram for all known discy YSOs with available NIR information (Fig. 6) further shows that *Chandra* did not detect many low-mass and/or highly obscured discy stars identified by means of *Spitzer* data. For the analysis of the stellar population inside the globule, a region where *Chandra*'s sensitivity deteriorates, we rely heavily on the *Spitzer* catalogue of discy stars from MC09.

There are 18 X-ray-selected discless stars and 45 IR-excess-selected and/or X-ray-selected disc-bearing stars projected against the globule (Table 3 here and table 2 from MC09). With the assumption that all of these observed stars are globule members, the apparent disc fraction averaged across the entire globule is 45/(18 + 45) or 70 per cent. 20 of the disc-bearing stars have been classified as Class I objects (MC09). The radiative transfer model fits to the optical–IR–radio band data of a MIR-selected sample of YSOs in the globule yield ages of $\lesssim$0.2 Myr and $\lesssim$1 Myr for the Class I and Class II objects, respectively (Reach et al. 2009). Considering the high apparent disc fraction, the high fraction of Class I objects, and the young ages derived for the selected sample of Class I/II YSOs by Reach et al. (2009), we reasonably assume an age $\lesssim$1 Myr for the entire population in the globule.

The IMF analysis here is restricted to the disc-bearing population in the globule. These are 38 out of 45 observed discy objects with available stellar mass estimates obtained from the J versus $J - H$ colour–magnitude diagram (Fig. 6). Their mass distribution is shown in Fig. 18. Despite the low counting statistics, the shape of the distribution is reminiscent of that of the Galactic field IMF. The IMF analysis gives a crude number on the total population of disc-bearing stars in the globule of ∼40 stars down to 0.1 M$_\odot$. This is likely a low limit because seven disc-bearing stars without *JHK* information have not been included in the analysis.

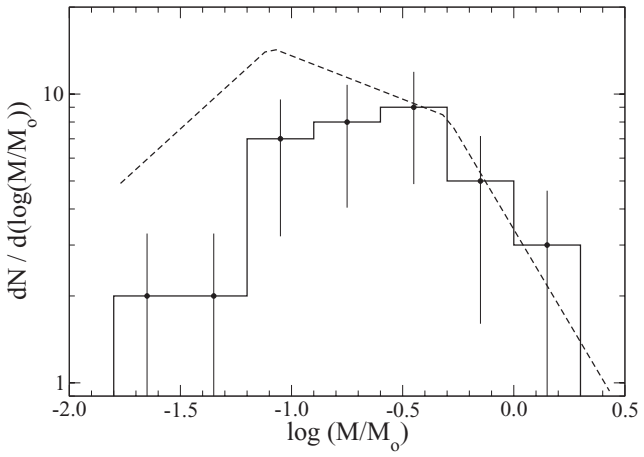

Figure 18. The mass distribution of discy stars found within the globule. The mass distribution of 38 young discy stars (36 from MC09 and additional two new from the X-ray catalogue) with available mass estimates, which lie projected against the globule, is shown as a solid histogram. The dashed line represents the scaled version of the Galactic field IMF (Kroupa 2002). The 1σ Poisson errors (Gehrels 1986) are also shown.

With respect to the discless population in the globule, 18 X-ray-selected discless stars projected against the globule have not been included in the IMF analysis. Out of these 18 X-ray stars, at least 10 have relatively high source extinctions, comparable to those of the disc-bearing population in the globule (Fig. 5). Assuming an age of 1 Myr, all 10 would have masses above 0.1 $M_\odot$. Thus, the total number of discy and discless stars in the part of the globule covered by the ACIS FOV is $\gtrsim$60.

8 IMPLICATIONS FOR TSF

8.1 Observational evidence for RDI TSF

Spatial-age gradients found in stellar populations in/around BRCs are often viewed as strong observational evidence for TSF. The youngest stars are typically embedded at the edge of the cloud facing the ionizing star, and older stars are aligned within and in front of the bright rim towards the ionizing star. For example, spatio-temporal gradients and TSF have been reported in BRCs and pillars on the edges of large H II regions in the Eagle Nebula (Sugitani et al. 2002), IC 1848 (Matsuyanagi et al. 2006; Ogura et al. 2007), IC 1396 (Getman et al. 2007; Ikeda et al. 2008; Choudhury et al. 2010), Sharpless 155 (Getman et al. 2009), Sharpless 171 and Sharpless 296 (Chauhan et al. 2009), and the Carina Nebula (Smith et al. 2010).

In Sections 5 and 6, we establish the spatio-temporal gradient of young stars from the centre of the IC 1396A cloud towards the HD 206267 O6.5f star. The identified stellar members are not uniformly distributed around the globule but rather are concentrated along the ionized rim, both outside (stellar groups 'G1'+'G2'+'G6'+'G7' in Fig. 13) and inside ('G3'+'G4') the cloud. The clustering of young stars in front of the cloud is also consistent with the previously reported arc-shaped layer of ∼20 low-mass, high-accretion stars from B11 and/or a dozen of ∼1 Myr optical stars from SA05. The stars located inside the cloud have typical ages of $\lesssim$1 Myr (Section 7.4), the stars found right in front of the cloud have typical ages of $\lesssim$2–3 Myr (Section 5), and the stars located farther to the east, in the Trumpler 37 cluster, are older with ages of $\gtrsim$3.5 Myr (Section 5). This age gradient is also consistent with our tentative finding that the apparent disc fraction is decreasing from 75 to 100 per cent inside the cloud cores, to 48 per cent in front of the cloud, and to 35 per cent farther to the east towards HD 206267 (Section 6).

The results from this work, combined with the results from the previous studies, thus provide strong evidence that the Trumpler 37/IC 1396A region possesses many of the observational features of an RDI TSF:

(i) The presence of an exciting star (HD 206267) and a BRC (IC 1396A) protruding inside the H II region and surrounded by an ionized rim (Rim A and Rim Aa) facing the exciting star (Fig. 1).

(ii) The presence of dense molecular cores close to the rim (Patel et al. 1995, their fig. 8) and (Weikard et al. 1996, their fig. 14a). This is consistent with the scenario where the expanding ionization front from HD 206267 penetrates the inter-core cloud region and drives shocks into the cores, compressing them sufficiently to trigger gravitational collapse.

(iii) A rough equilibrium between the H II pressure and the cloud pressure found at the interfaces between Rim A and the head of the IC 1396A globule (Reach et al. 2009), and Rim Aa and the SFO 36 cloud (Morgan et al. 2004). This indicates that the cloud could have been recently shocked by a photoionization shock. In addition, for the SFO 36 cloud, Morgan, Urquhart & Thompson (2009) and Morgan et al. (2010) measure relatively high values of CO excitation temperature and turbulent velocity dispersion, which are consistent with those of other shocked cloud candidates.

(iv) A clumpy spatial distribution of young stars both inside and in front of the cloud (Fig. 13) suggesting recent formation in distinct molecular cores. The proximity of the stars to the ionized rim immediately suggests a physical relationship between star formation and the ionization front propagating through the globule, and can be explained within the framework of the RDI model.

(v) The spatio-temporal gradient of young stars, both age and disc gradients, oriented towards the exciting star (Figs 12 and 13 here, fig. 11 in SA05, and fig. 18a in B11).

8.2 Contribution of TSF to the total population of the IC 1396 H II region

8.2.1 Motivation

The overall effect of TSF on the global star formation rate of the Galaxy is difficult to ascertain (Elmegreen 2011). A handful of studies attempted to estimate the effect. From an observational side, counting IRAS point sources embedded in BRCs of numerous H II regions, Sugitani et al. (1991) estimate the contribution of TSF from expanding H II regions to be only ∼5 per cent by mass of the stars in the Galaxy. Deharveng et al. (2010) find that 26 per cent of the MIR shells from the *Spitzer*-GLIMPSE survey harbour UCH II regions and/or methanol masers, likely indicating triggering of massive star formation. From comparison of positions of very young and massive stars identified in the RMS survey with respect to locations of numerous MIR shells from the *Spitzer*-GLIMPSE survey, Thompson et al. (2012) estimate the fraction of Galactic massive stars triggered by expanding H II regions to be 14–30 per cent.

From a theoretical perspective, by turning on and off an irradiation feedback on a turbulent 10^4 $M_\odot$ molecular cloud, Dale, Clark & Bonnell (2007b) find that TSF might increase the total amount of star formation by as much as 30 per cent. However, their SPH simulations show no observable characteristics for distinguishing

triggered from spontaneously formed stars. Although it is often difficult to make such a distinction in observational studies of individual H II regions, in Sections 8.1 and 8.2.2 we argue that an RDI triggered stellar population can be identified in the case of the Trumpler 37/IC 1396 A region. Hence, the contribution of TSF in the central part of the IC 1396 H II region, and with some additional assumptions in the entire H II region, can be estimated.

8.2.2 Contribution in the central part of the H II region

In Section 7, we establish the total populations of stars down to $0.1\,M_{\odot}$ for different areas of the region: ∼480 stars within the R15 area around HD 206267; ∼235–250 stars in the area outside the globule covered by the ACIS field; and $\gtrsim$60 YSOs inside the globule within the ACIS field. These numbers are employed here to estimate the input of TSF to the total population of the central part of the region.

Based on the arguments presented in Section 8.1, it is reasonable to propose that most of the YSOs inside the IC 1396A cloud and the bulk of the stars in the stellar groups 'G1'+ 'G2' + 'G6' + 'G7' (=G1267) in front of the cloud (Fig. 13) were formed through the RDI process. The notion is also consistent with our finding of a two-fold increase in the surface density of the optical SA05 stars at the western border of the central Trumpler 37 cluster (Section 6). Assuming that the two-fold increase is fully due to a triggered population, we obtain ∼20 per cent as a conservative estimate on the fraction of the old stellar members of Trumpler 37 within the G1267 group, which implies that ∼50 out of the 60 X-ray YSOs detected in G1267 have a triggered origin.

The total number of triggered stars in the G1267 group in front of the BRC is estimated to be $\sim 80 = 50 \times (235/146)$ stars down to $0.1\,M_{\odot}$, where ∼50 is the number of *Chandra*-observed triggered candidates in G1267, 146 is the number of *Chandra*-observed stars in the entire ACIS field outside the globule, and 235 is the inferred total number of stars in the entire ACIS field outside the globule. This number combined with the conservative (low limit) estimate on the total stellar population inside the globule ($\gtrsim$60 stars; Section 7.4) gives the total triggered population in IC 1396A of $\gtrsim$140 stars down to $0.1\,M_{\odot}$. This is likely a lower limit as we do not include possible contribution of the sparse group of stars with a high apparent disc fraction seen right in front of Rim Aa (Fig. 13c).

In contrast, the total population of the central Trumpler 37 cluster is $480 - 35/2/150 \times 480 = 424$ stars down to $0.1\,M_{\odot}$, where 480 is an estimate on the total stellar population within the R15 area around HD 206267, 35 and 150 are the numbers of the observed optical SA05 stars located within the overlap area 'C5' and the entire the R15 area, respectively, and 2 accounts for the increase in the surface density of the stars within the overlap area due to the presence of the triggered population. The contribution of the triggered stellar population to the total population of the central part of the IC 1396 H II region to date is thus $\gtrsim$25 per cent [$\gtrsim 140/(424 + 140)$].

8.2.3 Contribution for the entire H II region

A rough estimate of the contribution of TSF for the entire IC 1396 H II region can be further obtained by extrapolating our results for the triggered population in/around the IC 1396A cloud combined with the information on the low-mass, high-accretion stars from the survey of the entire IC 1396 H II region by B11. This requires the following additional assumptions. First, we assume that the total number of stars in the entire IC 1396 H II region is similar to that of the ONC. This is supported by the fact that they each have an equal number of stars B9 or earlier, and thus should have roughly the same total stellar populations.[10] Here we assume that the ONC population is 2800 stars (Hillenbrand & Hartmann 1998). Secondly, we assume that the birth of all low-mass, high-accretion B11 stars, which are found in clusters in front of the BRCs, was triggered. This is true for the ACIS field, where out of 22 B11 stars 21 are likely associated with the triggered population: 19 belong to the G1267 stellar group in/around Rim A, one is within the cloud's head, and the other one is right in front of Rim Aa. Based on fig. 9 from B11 we count >15 YSOs clustered in front of Rim E, about 10 stars in front of Rim B, several high-accretion stars in front of Rims J and H, and >10 stars in front of some other, unlabelled, BRCs, totalling >40 observed B11 triggered stars outside the ACIS field. Thirdly, we assume that the ratio of the number of the observed B11 triggered stars to the total number of the associated triggered stars, $R_{\rm t}$, is constant across the H II region. Within the ACIS field, $R_{\rm t} = 21/(>140) \sim 15$ per cent. The contribution of TSF for the entire H II region is then $\gtrsim$14 per cent [$(>40 + 21)/R_{\rm t}/2800$].

Combining this with the estimate for the central cluster in Section 8.2.2, $\gtrsim$14–25 per cent of the stars in the IC 1396 region have a triggered origin. This is consistent with the various observational and theoretical estimates reviewed in Section 8.2.1.

However, it has to be stressed that we are observing IC 1396 and other giant H II regions at only a single moment in their histories. IC 1396 has expanded to a radius 12 pc over few million years, and the H II shock likely triggered star formation in many now-dissipated molecular cloud cores. The H II region is likely to persist for several million years into the future with supernova remnant shocks in addition to UV radiation and OB wind shocks. These shocks will encounter more cores that are now embedded in the larger cloud. Thus, if the cluster can trigger 14–25 per cent of its population from the cloud cores that are active today, it seems plausible that it can trigger much more over the full lifetime of the H II region.

8.3 Other aspects of TSF

8.3.1 Star formation efficiency

Measured star formation efficiencies (SFEs) of entire giant molecular clouds typically vary from a few to several per cent (Evans et al. 2009, and references therein), whereas SFEs of embedded clusters associated with individual massive dense molecular cores are significantly higher ranging between 10 and 30 per cent (Lada & Lada 2003, and references therein).

For the total triggered population in/around IC 1396A of >140 stars, assuming an average mass of $\sim 0.5\,M_{\odot}$, consistent with a standard IMF, and adding individual masses of likely triggered high-mass B-type stars in the region, $\gtrsim 10\,M_{\odot}$ for the B3+B5 binary star HD 206081 (*Chandra* source #382) and several $M_{\odot}$ for the B3 star HD 239710 (*Chandra* source # 135; Fig. 13d), we obtain an estimated total triggered stellar mass of $M_{\rm star} \sim 90\,M_{\odot}$. The mass of the observed molecular gas in IC 1396A is only $M_{\rm gas} \sim 200\,M_{\odot}$ today (Patel et al. 1995; Weikard et al. 1996). The inferred

[10] From table 1 of Stelzer et al. (2005), the ONC has nine stars between B3 and O7 and five stars between B9 and B4. From table 5 of SA05 and adding HD 206267 and HD 206183, IC 1396 has three probable members between B3 and O6 and 13 between B9 and B4. So they each have ∼15 stars B9 or earlier. Furthermore, the most massive systems in both regions have similar spectral types – O6 star HD 206267 and O9.5 star HD 206183 in IC 1396 *versus* O6-7 star θ^1 Ori C and O9.5 star θ^2 Ori A in the ONC.

current SFE for the IC 1396A stellar population is thus $M_{\rm star}/(M_{\rm star} + M_{\rm gas}) \sim 30$ per cent at the top of the typical SFE range measured in other active star-forming regions.

Even higer SFEs of >40 per cent were recently reported in a number of cases of likely TSF, for example, Cep B/OB3b (Getman et al. 2009), Sh 2-233IR (Yan et al. 2010), L935/NGC 7000 (Toujima et al. 2011). However, the gas mass detected today could be only a fraction of the original cloud mass, so the SFE would be lower with respect to the original gas mass. Thus, the high values of apparent SFE in IC 1396A and the other regions of TSF indicate either an efficient star formation or an efficient removal of molecular gas by photoevaporation and stellar winds.

8.3.2 Long-lived RDI triggering in a clumpy cloud

Intermediate-mass stars are often born surrounded by small groups of a few to a few dozen lower mass PMS stars (Testi, Palla & Natta 1999; Adams & Myers 2001). The stellar group 'G2' is composed of $\gtrsim$15 YSOs around the B3+B5 binary system HD 206081 (Figs 13c and d). The high apparent disc fraction of ∼60 per cent, the presence of six high-accretion YSO systems from B11, and the filamentary structure seen at 24 μm coincident with the stellar group suggest that the group was formed very recently. The projected distance between 'G2' and the stellar group 'G1', located right along optical Rim A, is 1.5 pc. Theoretically, it is possible that stars recently formed in 'G1' having acquired velocity dispersion $\gtrsim$1 km s^{-1} have drifted 1–2 pc in all directions, populating the field around 'G1' including the location of 'G2' with triggered stars. However, the distinct appearance of the two groups, and the notion of simultaneous formation of intermediate-mass stars and PMS siblings, favours the view that the star drift does not play an important role here and that the present locations of the two groups are directly associated with locations of their distinct parental molecular cores. This is analogous to the current state of the IC 1396A cloud, where the two distinct stellar groups 'G3' and 'G4' inside the cloud are each associated with its own molecular core.

This implies continuing star formation over millions of years when the RDI mechanism occurs in a larger than the presently seen IC 1396A cloud composed of multiple clumps. This view is consistent with the recent global picture of an H II region expanding into a non-uniform clumpy molecular cloud, where TSF would take place through simultaneous enhancement of density and global radiation driven implosion of numerous pre-existing molecular clumps (Walch et al. 2011).

9 CONCLUSIONS

Signatures of small-scale TSF on the periphery of H II regions can be erased on short time-scales and thus, it is often difficult to identify sites of TSF and to measure the impact of triggering processes. There are only a handful of studies in the literature that have attempted to estimate the contribution of TSF from expanding H II regions. IR-emitting protostars in cloud cores and larger populations of PMS stars with spatial gradients in stellar age indicative of long-standing triggering processes have both been seen associated with several clouds on the periphery of expanding H II regions. Much of the progress is due to the fruitful combination of X-ray and optical/IR surveys; the former captures the older discless PMS population, while the latter detects the discy and accretion population.

IC 1396 is a nearby, large shell-like H II region, where traces of recent TSF are still evident. We present new *Chandra* X-ray data and auxiliary IR *Spitzer* and optical FLWO/LAICA data of YSOs associated with the central cluster Trumpler 37 and the adjacent BRC IC 1396A. These data are merged with the data from previously published optical–IR stellar catalogues of the region. The goal of this work is to identify, understand and quantify the triggered stellar population in the region associated with the IC 1396A cloud and to estimate the contribution of TSF to the entire H II region.

Out of 415 X-ray sources detected in the Trumpler 37/IC 1396A area, 175 are identified as YSOs and classified on 124 discless and 51 discy objects (Section 3). The majority of the remaining X-ray sources are contaminants, mainly extragalactic sources unrelated to the region (Section 3.2). In addition to the 175 X-ray-emitting YSOs, we identify 42 non-*Chandra*, IR-excess, low-mass members of the region (Section 4). Combining these data with the previous optical (SA05; B11) and IR (MC09) catalogues of YSOs yields a total of 259 YSOs in/around the IC 1396A cloud within the ACIS field, half of which are new members discovered in this work (Section 6).

The age and spatial distributions of young stars reveal a spatio-temporal gradient of stars from the IC 1396A cloud towards the primary ionizing star HD 206267 (Sections 5 and 6). Young stars are found to be clustered along the ionized rim, both outside and inside the cloud. The clustering of young stars in front of the cloud is consistent with the previously reported arc-shaped layer of the low-mass, high-accretion stars (B11) and/or the ∼1 Myr old optical stars (SA05). Quantitatively, the number of stars clustered in front of the cloud is consistent with the two-fold increase in the stellar surface density at the western border of the central Trumpler 37 cluster (Sections 6 and 8.2.2). The stellar age increases from $\lesssim$1 Myr inside the cloud, to <2–3 Myr in front of the cloud, to ∼4 Myr towards the central Trumpler 37 cluster. Combined with the results from the previous studies, these findings provide strong evidence for RDI TSF over millions of years in the Trumpler 37/IC 1396A region (Section 8.1). Based on this evidence, we believe that the majority of the YSOs found inside the cloud and the majority of the stars found clustered in front of the cloud were likely formed through the RDI process extending over 2–3 Myr.

By scaling the XLF/IMF measurements obtained for different YSO samples in the region (Section 7) to the number of the observed triggered stars, we estimate a total of >140 triggered stars down to 0.1 $M_\odot$ in/around the IC 1396A cloud, constituting $\gtrsim$25 per cent of the total population in the central part of the region today (Section 8.2.2). Furthermore, with a few additional assumptions we estimate the contribution of the triggered stellar population to the total population of the entire IC 1396 H II region to be >14 per cent (Section 8.2.3). Thus, the currently active clouds on the periphery of IC 1396 add at least 14–25 per cent to the current cluster population. When past and future clouds are considered, the contribution of triggering to the star formation in the molecular cloud could be much higher.

The inferred apparent value of SFE for the triggered population in IC 1396A is 30 per cent using current gas cloud masses (Section 8.3.1). Our findings support a picture of continuing star formation over millions of years when the RDI mechanism occurs in a larger than the presently seen IC 1396A cloud composed of multiple clumps (Section 8.3.2).

ACKNOWLEDGMENTS

We thank the anonymous referee for helpful comments. We thank Leisa Townsley (Pennsylvania State University) for her role and financial support in the development of the wide variety of

Chandra-ACIS data reduction and analysis techniques and tools used in this study. We thank Kevin Luhman (Pennsylvania State University) for assistance with *Spitzer*-IRAC data analysis. We thank Robert Gutermuth (University of Massachusetts) for the development of *Spitzer* data analysis tools. We benefited from scientific discussions with Matt Povich and Leisa Townsley (Penn State). This work is supported by the *Chandra*-ACIS Team (PI: G. Garmire) through the SAO grant SV4-74018 and by the Chandra GO grant SAO # GO0-11027X (PI: K. Getman). AS acknowledges support from the Spanish 'Ramon y Cajal' programme. The Center for Exoplanets and Habitable Worlds is supported by the Pennsylvania State University, the Eberly College of Science, and the Pennsylvania Space Grant Consortium. This work is based on observations made with the *Spitzer Space Telescope*, which is operated by the Jet Propulsion Laboratory, California Institute of Technology, under a contract with NASA. We also use data products of the Two-Micron All-Sky Survey, which is a joint project of the University of Massachusetts and the Infrared Processing and Analysis Center/California Institute of Technology, funded by NASA and NSF.

REFERENCES

Adams F. C., Myers P. C., 2001, ApJ, 553, 744
Allen L. E. et al., 2004, ApJS, 154, 363
Baraffe I., Chabrier G., Allard F., Hauschildt P. H., 1998, A&A, 337, 403
Baraffe I., Chabrier G., Gallardo J., 2009, ApJ, 702, L27
Barentsen G. et al., 2011, MNRAS, 415, 103 (B11)
Beltrán M. T., Massi F., López R., Girart J. M., Estalella R., 2009, A&A, 504, 97
Bessell M. S., Brett J. M., 1988, PASP, 100, 1134
Bisbas T. G., Wünsch R., Whitworth A. P., Hubber D. A., Walch S., 2011, ApJ, 736, 142
Broos P. S., Feigelson E. D., Townsley L. K., Getman K. V., Wang J., Garmire G. P., Jiang Z., Tsuboi Y., 2007, ApJS, 169, 353
Broos P. S., Townsley L. K., Feigelson E. D., Getman K. V., Bauer F. E., Garmire G. P., 2010, ApJ, 714, 1582
Broos P. S. et al., 2011, ApJS, 194, 2
Broos P. S., Townsley L. K., Getman K. V., Bauer F. E., 2012, Astrophysics Source Code Library, record ascl:1203.001, 3001
Burgasser A. J., Kirkpatrick J. D., Reid I. N., Brown M. E., Miskey C. L., Gizis J. E., 2003, ApJ, 586, 512
Burningham B., Naylor T., Littlefair S. P., Jeffries R. D., 2005, MNRAS, 363, 1389
Caramazza M. et al., 2012, A&A, 539, A74
Chauhan N., Pandey A. K., Ogura K., Ojha D. K., Bhatt B. C., Ghosh S. K., Rawat P. S., 2009, MNRAS, 396, 964
Chauhan N., Ogura K., Pandey A. K., Samal M. R., Bhatt B. C., 2011, PASJ, 63, 795
Choudhury R., Mookerjea B., Bhatt H. C., 2010, ApJ, 717, 1067
Churchwell E. et al., 2006, ApJ, 649, 759
Contreras M. E., Sicilia-Aguilar A., Muzerolle J., Calvet N., Berlind P., Hartmann L., 2002, AJ, 124, 1585
Dale J. E., Bonnell I. A., Whitworth A. P., 2007a, MNRAS, 375, 1291
Dale J. E., Clark P. C., Bonnell I. A., 2007b, MNRAS, 377, 535
Deharveng L., Lefloch B., Zavagno A., Caplan J., Whitworth A. P., Nadeau D., Martin S., 2003, A&A, 408, L25
Deharveng L. et al., 2010, A&A, 523, A6
Eckart M. E., McGreer I. D., Stern D., Harrison F. A., Helfand D. J., 2010, ApJ, 708, 584
Elmegreen B. G., 2011, EAS Publications Series. EAS, EDP Sciences, France, p. 45
Elmegreen B. G., Lada C. J., 1977, ApJ, 214, 725
Elmegreen B. G., Palous J., eds, 2007, Proc. IAU Symp. 237, Triggered Star Formation in a Turbulent ISM. Cambridge Univ. Press, Cambridge, p. 1
Evans N. J., II et al., 2009, ApJS, 181, 321
Fazio G. G. et al., 2004, ApJS, 154, 10
Feigelson E. D., 2010, Publ. Natl. Acad. Sci., 107, 7153
Feigelson E. D., Getman K. V., 2005, in Corbelli E., Palla F., Zinnecker H., eds, The Initial Mass Function: 50 Years Later. Springer, Dordrecht, p. 163
Feigelson E. D. et al., 2005, ApJS, 160, 379
Flaherty K. M., Pipher J. L., Megeath S. T., Winston E. M., Gutermuth R. A., Muzerolle J., Allen L. E., Fazio G. G., 2007, ApJ, 663, 1069
Freeman P. E., Kashyap V., Rosner R., Lamb D. Q., 2002, ApJS, 138, 185
Froebrich D., Scholz A., Eislöffel J., Murphy G. C., 2005, A&A, 432, 575
Garmire G. P., Bautz M. W., Ford P. G., Nousek J. A., Ricker G. R., 2003, in Truemper J. E., Tananbaum H. D., eds, Proc. SPIE Vol. 4851, X-Ray and Gamma-Ray Telescopes and Instruments for Astronomy. SPIE, Bellingham, p. 28
Gehrels N., 1986, ApJ, 303, 336
Getman K. V. et al., 2005, ApJS, 160, 319
Getman K. V., Feigelson E. D., Townsley L., Broos P., Garmire G., Tsujimoto M., 2006, ApJS, 163, 306
Getman K. V., Feigelson E. D., Garmire G., Broos P., Wang J., 2007, ApJ, 654, 316
Getman K. V., Feigelson E. D., Luhman K. L., Sicilia-Aguilar A., Wang J., Garmire G. P., 2009, ApJ, 699, 1454
Getman K. V., Feigelson E. D., Broos P. S., Townsley L. K., Garmire G. P., 2010, ApJ, 708, 1760
Getman K. V. et al., 2011, ApJS, 194, 3
Gritschneder M., Burkert A., Naab T., Walch S., 2010, ApJ, 723, 971
Gutermuth R. A. et al., 2008, ApJ, 674, 336
Gutermuth R. A., Megeath S. T., Myers P. C., Allen L. E., Pipher J. L., Fazio G. G., 2009, ApJS, 184, 18
Hartmann L., 2003, ApJ, 585, 398
Hartmann L., Megeath S. T., Allen L., Luhman K., Calvet N., D'Alessio P., Franco-Hernandez R., Fazio G., 2005, ApJ, 629, 881
Hessman F. V., Beckwith S. V. W., Bender R., Eisloeffel J., Goetz W., Guenther E., 1995, A&A, 299, 464
Hillenbrand L. A., Hartmann L. W., 1998, ApJ, 492, 540
Hosokawa T., Inutsuka S.-i., 2006, ApJ, 646, 240
Ikeda H. et al., 2008, AJ, 135, 2323
Kessel-Deynet O., Burkert A., 2003, MNRAS, 338, 545
Kraus A. L., Hillenbrand L. A., 2009, ApJ, 704, 531
Kroupa P., 2002, Sci, 295, 82
Kuhn M. A., Getman K. V., Feigelson E. D., Reipurth B., Rodney S. A., Garmire G. P., 2010, ApJ, 725, 2485
Kun M., Kiss Z. T., Balog Z., 2008, in Reipurth B., ed., Handbook of Star Forming Regions: Volume I. Astron. Soc. Pac., San Francisco, p. 136
Lada C. J., Lada E. A., 2003, ARA&A, 41, 57
Lada C. J. et al., 2006, AJ, 131, 1574
Lawson W. A., Lyo A.-R., Bessell M. S., 2009, MNRAS, 400, L29
Li J., Kastner J. H., Prigozhin G. Y., Schulz N. S., Feigelson E. D., Getman K. V., 2004, ApJ, 610, 1204
Luhman K. L., Hernández J., Downes J. J., Hartmann L., Briceño C., 2008, ApJ, 688, 362
Luhman K. L., Allen P. R., Espaillat C., Hartmann L., Calvet N., 2010, ApJS, 186, 111
Matsuyanagi I., Itoh Y., Sugitani K., Oasa Y., Mukai T., Tamura M., 2006, PASJ, 58, L29
Mayne N. J., Naylor T., Littlefair S. P., Saunders E. S., Jeffries R. D., 2007, MNRAS, 375, 1220
Megeath S. T. et al., 2004, ApJS, 154, 367
Mercer E. P., Miller J. M., Calvet N., Hartmann L., Hernandez J., Sicilia-Aguilar A., Gutermuth R., 2009, AJ, 138, 7
Meyer M. R., Calvet N., Hillenbrand L. A., 1997, AJ, 114, 288
Miao J., White G. J., Thompson M. A., Nelson R. P., 2009, ApJ, 692, 382
Mizuta A., Kane J. O., Pound M. W., Remington B. A., Ryutov D. D., Takabe H., 2006, ApJ, 647, 1151
Morales-Calderón M. et al., 2009, ApJ, 702, 1507 (MC09)
Morgan L. K., Thompson M. A., Urquhart J. S., White G. J., Miao J., 2004, A&A, 426, 535

Morgan L. K., Urquhart J. S., Thompson M. A., 2009, MNRAS, 400, 1726
Morgan L. K., Figura C. C., Urquhart J. S., Thompson M. A., 2010, MNRAS, 408, 157
Mucciarelli P., Preibisch T., Zinnecker H., 2011, A&A, 533, A121
Nisini B. et al., 2001, A&A, 376, 553
Ogura K., Sugitani K., Pickles A., 2002, AJ, 123, 2597
Ogura K., Chauhan N., Pandey A. K., Bhatt B. C., Ojha D., Itoh Y., 2007, PASJ, 59, 199
Patel N. A., Goldsmith P. F., Snell R. L., Hezel T., Xie T., 1995, ApJ, 447, 721
Preibisch T., 2012, Res. Astron. Astrophys., 12, 1
Preibisch T., Feigelson E. D., 2005, ApJS, 160, 390
Preibisch T. et al., 2005, ApJS, 160, 401
Prisinzano L. et al., 2008, ApJ, 677, 401
Reach W. T. et al., 2004, ApJS, 154, 385
Reach W. T. et al., 2005, PASP, 117, 978
Reach W. T. et al., 2009, ApJ, 690, 683
Robin A. C., Reylé C., Derrière S., Picaud S., 2003, A&A, 409, 523
Schneider N. et al., 2011, A&A, 529, A1
Schwartz R. D., Wilking B. A., Giulbudagian A. L., 1991, ApJ, 370, 263
Sicilia-Aguilar A., Hartmann L. W., Briceño C., Muzerolle J., Calvet N., 2004, AJ, 128, 805
Sicilia-Aguilar A., Hartmann L. W., Hernández J., Briceño C., Calvet N., 2005, AJ, 130, 188 (SA05)
Sicilia-Aguilar A. et al., 2006, ApJ, 638, 897 (SA06)
Sicilia-Aguilar A., Henning T., Hartmann L. W., 2010, ApJ, 710, 597
Sicilia-Aguilar A., Henning T., Dullemond C. P., Patel N., Juhasz A., Bouwman J., Sturm B., 2011, ApJ, 742, 39
Siess L., Dufour E., Forestini M., 2000, A&A, 358, 593
Simpson R. J. et al., 2012, MNRAS, 424, 2442
Smith N. et al., 2010, MNRAS, 406, 952
Soderblom D. R., 2010, ARA&A, 48, 581
Stelzer B., Flaccomio E., Montmerle T., Micela G., Sciortino S., Favata F., Preibisch T., Feigelson E. D., 2005, ApJS, 160, 557
Stelzer B., Preibisch T., Alexander F., Mucciarelli P., Flaccomio E., Micela G., Sciortino S., 2012, A&A, 537, A135
Sugitani K., Fukui Y., Ogura K., 1991, ApJS, 77, 59
Sugitani K., Tamura M., Ogura K., 1995, ApJ, 455, L39
Sugitani K. et al., 2002, ApJ, 565, L25
Telleschi A., Güdel M., Briggs K. R., Audard M., Palla F., 2007, A&A, 468, 425
Testi L., Palla F., Natta A., 1999, A&A, 342, 515
Thompson M. A., Urquhart J. S., Moore T. J. T., Morgan L. K., 2012, MNRAS, 421, 408
Toujima H., Nagayama T., Omodaka T., Handa T., Koyama Y., Kobayashi H., 2011, PASJ, 63, 1259
Urquhart J. S., Morgan L. K., Thompson M. A., 2009, A&A, 497, 789
Walch S., Whitworth A., Bisbas T., Hubber D. A., Wuensch R., 2011, preprint (arXiv:1109.3478)
Wang J., Townsley L. K., Feigelson E. D., Getman K. V., Broos P. S., Garmire G. P., Tsujimoto M., 2007, ApJS, 168, 100
Wang J., Townsley L. K., Feigelson E. D., Broos P. S., Getman K. V., Roman-Zuniga C. G., Lada E., 2008, ApJ, 675, 464
Wang J., Feigelson E. D., Townsley L. K., Broos P. S., Roman-Zuniga C. G., Lada E., Garmire G., 2010, ApJ, 716, 474
Wang J. et al., 2011, ApJS, 194, 11
Weikard H., Wouterloot J. G. A., Castets A., Winnewisser G., Sugitani K., 1996, A&A, 309, 581
Weisskopf M. C., Brinkman B., Canizares C., Garmire G., Murray S., Van Speybroeck L. P., 2002, PASP, 114, 1
Whalen D. J., Norman M. L., 2008, ApJ, 672, 287
Whitworth A. P., Bhattal A. S., Chapman S. J., Disney M. J., Turner J. A., 1994, MNRAS, 268, 291
Wolk S. J. et al., 2011, ApJS, 194, 12
Yan C.-H., Minh Y. C., Wang S.-Y., Su Y.-N., Ginsburg A., 2010, ApJ, 720, 1
Zacharias N., Monet D. G., Levine S. E., Urban S. E., Gaume R., Wycoff G. L., 2004, BAAS, 36, 1418
Zavagno A., Deharveng L., Comeron F., Brand J., Massi F., Caplan J., Russeil D., 2006, A&A, 446, 171
Zavagno A., Pomares M., Deharveng L., Hosokawa T., Russeil D., Caplan J., 2007, A&A, 472, 835

SUPPORTING INFORMATION

Additional Supporting Information may be found in the online version of this article:

Table 1. Basic X-ray source properties.
Table 2. Optical and IR photometry of X-ray sources.
Table 3. Derived properties, stellar identifications, membership and classification.

Please note: Wiley-Blackwell are not responsible for the content or functionality of any supporting materials supplied by the authors. Any queries (other than missing material) should be directed to the corresponding author for the article.

This paper has been typeset from a TEX/LATEX file prepared by the author.